



## Automated identification of local contamination in remote atmospheric composition time series

Ivo Beck<sup>1</sup>, H el ene Angot<sup>1</sup>, Andrea Baccharini<sup>1</sup>, Lubna Dada<sup>1</sup>, Lauriane Qu el ever<sup>2</sup>, Tuija Jokinen<sup>2,3</sup>, Tiia Laurila<sup>2</sup>, Markus Lampim aki<sup>2</sup>, Nicolas Bukowiecki<sup>4</sup>, Matthew Boyer<sup>2</sup>, Xianda Gong<sup>5</sup>, Martin Gysel-Beer<sup>6</sup>, Tuukka Pet aj a<sup>2</sup>, Jian Wang<sup>5</sup>, and Julia Schmale<sup>1\*</sup>

<sup>1</sup>Extreme Environments Research Laboratory,  cole Polytechnique f ed erale de Lausanne, Switzerland

<sup>2</sup>Institute for Atmospheric and Earth System Research, INAR/Physics, FI-00014 University of Helsinki, Finland

<sup>3</sup>Climate & Atmosphere Research Centre (CARE-C), The Cyprus Institute, P.O. Box 27456, Nicosia, 1645, Cyprus

<sup>4</sup>Atmospheric Sciences, Department of Environmental Sciences, University of Basel, Switzerland

10 <sup>5</sup>Center for Aerosol Science and Engineering, Department of Energy, Environmental and Chemical Engineering, Washington University in St. Louis, St. Louis, MO, USA

<sup>6</sup>Laboratory of Atmospheric Chemistry, Paul Scherrer Institute, Villigen PSI, Switzerland

\*Correspondence to: Julia Schmale ([julia.schmale@epfl.ch](mailto:julia.schmale@epfl.ch)), Ivo Beck ([ivo.beck@epfl.ch](mailto:ivo.beck@epfl.ch))



## 15 **Abstract.**

Atmospheric observations in remote locations offer a possibility to explore trace gas and particle concentrations in pristine environments. However, data from remote areas are often contaminated by pollution from local sources. Detecting this pollution is thus a central and frequently encountered issue. Consequently, many different methods exist today to identify local pollution in atmospheric composition measurement time series, but no single method has been widely accepted. In this study, we present a new method to identify primary pollution in remote atmospheric datasets, e.g., from ship campaigns or stations with low background signal compared to the pollution signal. The Pollution Detection Algorithm (PDA) identifies and flags periods of polluted data in five steps. The first and most important step identifies polluted periods based on the gradient (time-derivative) of a concentration over time. If this gradient exceeds a given threshold, data are flagged as polluted. Further pollution identification steps are a simple concentration threshold filter, a neighboring points filter (optional), a median and a sparse data filter (optional). The PDA only relies on the target dataset itself and is independent of ancillary datasets such as meteorological variables. All parameters of each step are adjustable so that the PDA can be “tuned” to be more or less stringent (e.g., flag more or less data points as polluted).

The PDA was developed and tested with a particle number concentration dataset collected during the Multidisciplinary drifting Observatory for the Study of Arctic Climate (MOSAiC) expedition in the Central Arctic. Using strict settings, we identified 62 % of the data as influenced by local pollution. Using a second independent particle number concentration dataset also collected during MOSAiC, we evaluated the performance of the PDA against the same dataset cleaned by visual inspection. The two methods agreed in 94 % of the cases. Additionally, the PDA was successfully applied on a trace gas dataset (CO<sub>2</sub>), also collected during MOSAiC, and on another particle number concentration dataset, collected at the high altitude background station Jungfraujoch, Switzerland. Thus, the PDA proves to be a useful and flexible tool to identify periods affected by local pollution in atmospheric composition datasets without the need for ancillary measurements. It is best applied to data representing primary pollution. The user-friendly and open access code enables reproducible application to a wide suite of different datasets. It is available at: <https://doi.org/10.5281/zenodo.5761101>.

## 1 **Introduction**

Aerosol and trace gas measurements in remote environments, such as polar or high altitude regions, are essential to improve our understanding of key climate and biogeochemical processes and to constrain numerical models (Carslaw et al., 2010; Bukowiecki et al., 2016; Reddington et al., 2017). A major challenge associated with obtaining atmospheric composition measurements in such locations is that data are often impacted by emissions from local activities, which are not representative of the remote environment and interfere with the observation and data analysis objectives (Bukowiecki et al., 2021). Such local pollution emissions can originate from the measurement platform itself, e.g., research vessels (Schmale et al., 2019; Baccarini et al., 2020; Humphries et al., 2016), or from touristic (Bukowiecki et al., 2021), local anthropogenic (Asmi et al., 2016) or nearby industrial (Kolesar et al., 2017) activities. Local emissions often originate from combustion processes and can directly



affect trace gas mixing ratios (hereafter referred to as concentrations), aerosol concentrations, and other particle properties. For subsequent analysis, the influence of local pollution must be correctly detected to separate polluted from unaffected data. Local pollution influence is typically characterized by enhanced particle or trace gas concentrations and strong variations in the signal amplitude on time scales varying between a few seconds (Bukowiecki et al., 2021; Baccarini et al., 2020) to several hours, depending on the nature of the emitting activity and wind direction. Pollution “spikes” disturb the measurement of the regional or remote background concentrations, which are inherently continuous and vary over time due to meteorological factors such as the boundary layer evolution (Bukowiecki et al., 2021), synoptic situations (Alroe et al., 2020) or relatively slow natural processes such as marine biogenic emissions (Frossard et al., 2014) or sea ice related new particle formation (Baccarini et al., 2020).

Numerous atmospheric composition measurements have been conducted in remote environments, such as the Arctic (Leck et al., 1996; Uttal et al., 2002; Tjernström et al., 2014) and the Southern Ocean (McFarquhar et al., 2021; Schmale et al., 2019), or at regional background sites around the Arctic (Uttal et al., 2016; Freud et al., 2017) or throughout Europe as part of the established monitoring network Aerosols, Clouds, and Trace gases Research Infrastructure (ACTRIS) (Herrmann et al., 2015; Asmi et al., 2013; Bukowiecki et al., 2021). Different approaches have been applied to detect and remove polluted data from these measurement sites. In one approach, Herrmann et al. (2015) removed polluted data based on visual inspection of the submicron particle size distribution spectra. Other approaches are based on the application of statistical filters that identify pollution based on outliers that deviate from a curve fitted to the data. Bukowiecki et al. (2002) developed a method for aerosols based on the 5<sup>th</sup> percentile within each minute, assuming it reflects uncontaminated background concentrations. This method has the caveat that for times without contamination, the background is biased low, while for highly contaminated data, the background is biased high. Ruckstuhl et al. (2012) assumed that a trace gas background signal is a combination of a baseline signal with the contribution of pollution. The background signal is estimated by applying a linear regression. The outliers are detected as the data points that exceed the estimated background by a factor of  $3\sigma$ . This method is called ‘robust extraction of baseline signal’ (REBS). El Yazidi et al. (2018) applied the REBS method to four datasets of trace gas measurements and compared it to the standard deviation method for particles (Drewnick et al., 2012), which detects pollution as data points that differ by more than  $3\sigma$  from the median of the data. Most recently, Bukowiecki et al. (2021) developed a new spike detection method for regional background observations. First, a signal baseline was determined for the 1-min total particle number concentration data based on a running 5<sup>th</sup> percentile, with an optimized time window and percentile threshold. This baseline was then subtracted from the original time series to isolate spikes in the time series. Finally, a spike flag was applied by removing data when the 1-min spike time series exceeded the 80<sup>th</sup> percentile of the surrounding 1-h time window by a user-defined fixed threshold. Generally, such statistical methods are not suited to reveal background signals at times when they are dominated by non-background signals, because this carries a risk that the non-background signals are falsely included in the background signals (Ruckstuhl et al., 2012).

Another commonly used pollution filtering method is based on wind direction. In this case, a pollution source sector can be defined to flag all time periods in a dataset with wind coming from this sector; winds from outside the source sector are



assumed to be pollution free (Leck et al., 1996; Asmi et al., 2016; Kyrö et al., 2013). For the Arctic Summer Cloud Ocean Study in 2008 on the Swedish icebreaker Oden, the measurement of a pollution tracer (toluene) was used in addition to a wind filter. If the toluene concentration running mean exceeded a threshold, the data were flagged as polluted (Tjernström et al., 2014). Toluene concentration measurements require complex instrumentation and are therefore not routinely observed. An inherent limitation of wind filters is that they cannot take into account the effect of recirculation of the emitted pollution, which can lead to contaminated measurements from different wind sectors. Humphries et al. (2019) used a combination of a carbon monoxide (CO) concentration threshold with a statistical filter applied to carbon dioxide (CO<sub>2</sub>) and black carbon (BC) data to clean particle number concentration and cloud condensation nuclei datasets. Data were collected on the Australian research vessel *Investigator* in 2016 in the Tasman Sea. The statistical filter flags the data points that deviate from the 5-min mean of each variable by a certain threshold. Additionally, a window filter was applied that sums all data points in a 20 min time window. If the sum of the polluted data points surpassed 10 % of the data points in the time window in one of the three datasets (CO, CO<sub>2</sub> or BC), all data points within this time window were flagged as polluted. Similarly, Schmale et al. (2019) and Moallemi et al. (2021) used a combination of CO<sub>2</sub> and particle number concentration data to detect contamination from ship exhaust. A binomial smoothing was applied to each time series, and when the ratio of the smoothed data over the original time series exceeded certain thresholds, the data were flagged as polluted.

The above examples demonstrate that there are many different ways of detecting local pollution in a dataset and that no single method has established itself and is widely used. While custom-made methods have the advantage that they are designed to work particularly well for a specific dataset, they have the disadvantage that they cannot necessarily be applied to other datasets, because they rely on ancillary information that might not be readily available at all measurement sites. This means that pollution-detection methods are not always reproducible and make comparison between cleaned datasets more challenging. Therefore, a common filtering method, which relies on a minimal number of input variables, is desirable to achieve reproducible pollution detection across a variety of datasets.

Here, we propose an algorithm to clean up particle number concentrations, particle number size distribution and trace gas concentration datasets collected at remote or background sites that experience random influence from local primary pollution sources. This method only requires a time series of the target particle number or trace gas concentration data and is independent of ancillary datasets such as BC or meteorological variables. As a result, the method can be applied to a large number of measurement sites. We embedded the algorithm in a user-friendly python-based code. The algorithm detects polluted periods in five steps. To increase the usability of this algorithm, the parameters can be “tuned” to adapt to different datasets, ambient conditions and requirements.

After introducing the PDA in detail in the methods, we evaluate its performance in the results section in three steps. First, the general evaluation is based on particle number concentration data measured during the MOSAiC expedition (Multidisciplinary drifting Observatory for the Study of Arctic Climate) between September 2019 and October 2020 (Shupe et al., under review). Second, we test results from the PDA against other common pollution identifying methods. Third, we evaluate its applicability



115 to further ship-based datasets such as aerosol number size distributions, aerosol mass composition, and trace gases concentrations, as well as to a particle number concentration dataset from a high altitude observatory.

## 2 Methods

In this section, we first present the datasets and instruments used for this study. In Sect. 2.2 and 2.3., we describe alternative filtering methods used to test the performance of the PDA. In Sect. 2.4., we describe the PDA with each of the five filtering steps in a dedicated subsection.

120 We developed and tested the PDA using atmospheric aerosol and trace gas concentrations measured in the *Swiss Container* during the year-long MOSAiC expedition in the central Arctic. The expedition started in September 2019 in Tromsø, Norway and ended in October 2020 in Bremerhaven, Germany, whereby the Research Vessel (RV) *Polarstern* (Alfred-Wegener-Institut Helmholtz-Zentrum für Polar- und Meeresforschung, 2017) drifted with sea ice in the central Arctic Ocean. The drift track is shown in Fig. A1. The aim of the expedition was to study sea ice, ecological, biogeochemical, ocean and atmospheric  
125 processes in the Arctic Ocean. A research camp was set up on the ice around the ship. A comprehensive introduction to the atmospheric measurements carried out during the expedition is presented in Shupe et. al. (under review). The *Swiss Container* was placed on the D-deck of the ship (see Fig. A2) to monitor the aerosol and gas phase atmospheric composition. Aerosols and trace gases were sampled from two different inlets: (i) a whole air inlet (total inlet) which allowed sampling all particles and droplets up to 40  $\mu\text{m}$  and (ii) an interstitial inlet equipped with a cyclone to cut off particles larger than 1  $\mu\text{m}$ , designed to  
130 sample particles that do not activate in cloud and fog (Fig. A3). The total inlet was built after the Global Atmosphere Watch recommendations (World Meteorological Organization, 2016). An automated valve inside the container switched hourly between the total and interstitial inlets to allow instruments connected behind the valve to sample from each of the inlets alternately. The measurement setup and the instrumentation used during the expedition are shown in appendix A in Fig. A3. The flow of the inlets was kept constant at 10 (total inlet) and 16.7 L/min (interstitial inlet). The inlets above the container had  
135 a length of 1.5 m and sampled at a height of approximately 15 m above sea level. The temperature inside the *Swiss Container* was kept constant at 20°C. The sampled air was dried when entering the container due to the strong temperature gradient between outside and inside, but additional inline heating was applied when necessary. Relative humidity (RH) in the inlet lines was continuously measured and maintained below 40 %.

Aerosol and trace gas measurements were regularly impacted by a variety of local pollution sources (e.g., ship stack, snow  
140 groomers, diesel generators, helicopters, ship vents). Polluted periods varied in time from seconds up to hours or days and the intensity of contamination varied with the distance from and type of source and with the wind direction, wind speed and turbulent air motion around the ship.

To segregate polluted from unaffected data for final analysis, we developed an algorithm that detects and tags polluted periods independent of the pollution source's position relative to the measurement site. For the development of the PDA, we used a  
145 particle number concentration dataset. In the following subsections, we describe the methodology used to develop and evaluate the performance of the PDA.



## 2.1 Instruments and data

### 2.1.1 Particle number concentration data

We used a particle number concentration dataset collected with a condensation particle counter (CPC) model 3025 by TSI (referred to as CPC3025) to develop the PDA. The CPC3025 has a minimum detectable particle diameter (50% counting efficiency) of  $D_{p,50} = 3$  nm and a maximum detectable particle concentration of  $9.99 \times 10^4 \text{ cm}^{-3}$ . It collected data at 10 s intervals during the expedition. The instrument was connected to the interstitial inlet. The sample flow of the CPC was set to 0.3 L/min during the entire expedition and was checked daily. We performed weekly zero tests with High Efficiency Particulate Air (HEPA) filters.

In addition to the CPC3025, we used particle number concentration data from the Aerosol Observing System (AOS) to evaluate the performance of the PDA. It was operated as part of the United States Department of Energy Atmospheric Radiation Measurement (ARM) facility during the same expedition. The ARM AOSs are measurement containers capable of measuring a suite of aerosol microphysical and chemical properties in a standardized, field-deployable design. Only a brief summary of the AOS is given here; a more comprehensive overview of the ARM AOS design, instrumentation, deployment history, and measurement objectives for the different facilities can be found in Uin et al. (2019).

The AOS was also located on the D-deck, at the port side of the *Swiss Container*, 2 m away (see Fig. A2). The aerosol instrumentation inside the AOS sampled from a single, shared total aerosol inlet on top of the AOS container. The inlet itself was 5 m in length, the inlet height was approximately 18 m above sea level. The particle number concentration data in the AOS container was obtained from a CPC model 3772 from TSI (referred to as CPCf) with a minimum detectable particle diameter of  $D_{p,50} = 10$  nm (Kuang et al., 2021). It ran with a flow rate of 1 L/min, and a sampling resolution of 1 second. The air to the CPC was dried before sampling using a Nafion dryer. Weekly filter tests and daily flow rate checks were performed. The temperature inside the AOS was maintained between 18–22°C. The AOS inlet was equipped with a purge blower that was designed specifically for this campaign to prevent ship stack pollution from entering the instruments. The purge blower was set up to trigger automatically according to elevated carbon monoxide (CO) concentrations, which were measured from a separate sample line that was collocated with the aerosol inlet. The purge blower was able to provide a high flow rate of continuous particle-free air into the AOS inlet, effectively purging the inlet of ship stack pollution. However, due to relatively low sensitivity of CO concentrations to pollution from the ship stack plume (see Fig. A4), the automated triggering system did not work automatically as planned. Thus, the purge blower was turned on manually when the bow of the ship was exposed to pollution for extended periods of time. As a result, the ARM CPC datasets show periodic gaps during local pollution events, but there are still times when the datasets are influenced by local pollution and additional cleaning is required. Therefore, the ARM CPC datasets are well suited to test the performance of the PDA.

To test the broader applicability of the PDA to datasets from sites with different characteristics, we used a particle number concentration dataset collected at the high-altitude GAW and ACTRIS research station Jungfraujoch (JFJ) in the Swiss Alps (Bukowiecki et al., 2016). The station is located at 3580 m.a.s.l. In winter it often represents the remote European free



180 troposphere, while in warmer seasons, intrusions of boundary layer air masses are frequently observed (Herrmann et al., 2015). The site also is a touristic destination, meaning that local pollution affecting the measurements interferes with the aim to achieve unpolluted background measurements (Bukowiecki et al., 2021). Data were collected by a CPC model 3772 by TSI. The measurement setup is described in more detail by (Bukowiecki et al., 2021). The results of this application are presented in Sect. 3.4.4.

#### 185 **2.1.2 Particle number size distribution data**

Furthermore, we applied the PDA to a particle size distribution dataset collected by a Scanning Mobility Particle Sizer (SMPS). The custom built SMPS (Schmale et al., 2017) was located in the *Swiss Container* behind the switching valve and recorded the size distribution of particles between 17 and 600 nm with a time resolution of three minutes. We applied the PDA to the SMPS integrated particle number concentration. The results are presented in Sect. 3.1.2.

#### 190 **2.1.3 Aerosol chemical composition data**

In addition, we tested the performance of the PDA against the aerosol chemical composition dataset obtained by the High-Resolution Time-of-Flight Aerosol Mass Spectrometer (HR-ToF-AMS) from Aerodyne Research Inc., located in the *Swiss Container*. The AMS measures the chemical composition of non-refractory aerosols, i.e., species that evaporate at temperatures up to 600°C. It typically detects sulphate (SO<sub>4</sub><sup>2-</sup>), nitrate (NO<sub>3</sub><sup>-</sup>), ammonium (NH<sub>4</sub><sup>+</sup>), chloride (Cl<sup>-</sup>), and organics (DeCarlo et al., 2006) from particles in the size range 0.07 – 1 µm, defined by the type of aerodynamic lens. The AMS was operated behind  
195 the switching valve to sample both interstitial and total inlet aerosol populations. Here, we use the mass signal of the ion fragment C<sub>4</sub>H<sub>9</sub><sup>+</sup> at a mass to charge ratio of m/z = 57. This fragment is a typical indicator of fresh fossil fuel combustion (Enroth et al., 2016; Massoli et al., 2012) and has been used before to detect pollution in remote regions (Schmale et al., 2013). The results of the application of the PDA on the chemical composition data will be discussed in Sect. 3.4.2.

#### 200 **2.1.4 Trace gas data**

We also used trace gas data collected in the *Swiss Container* to test the algorithm on datasets other than particle number concentration (Sect. 3.4.3). A detailed description of trace gas measurements during the MOSAiC expedition is given in Angot et al. (in prep.). Briefly, carbon dioxide (CO<sub>2</sub>), methane (CH<sub>4</sub>), and CO ambient air mixing ratios were monitored by cavity ring-down spectroscopy using a Picarro instrument (model G2401) behind the interstitial inlet. Regular calibrations were  
205 carried out during the expedition with gas mixtures of known CO<sub>2</sub>, CH<sub>4</sub> and CO mixing ratios. As described in Angot et al. (in prep.), nitric oxide (NO) ambient air concentrations were measured in a different container (University of Colorado) with a custom-built single-channel chemiluminescence analyzer (Fontijn et al., 1970), which was regularly calibrated by dynamic dilution of a 1.5 ppm compressed NO gas standard.



### 2.1.5 Wind data

210 Wind speed and direction were measured with a 2D sonic anemometer on the main mast of RV *Polarstern*. We used this wind dataset at a time resolution of 1 minute in this study (Schmithuesen, 2021a, b, c, d, e).

### 2.2 Wind based filtering method

The main source of local pollution during the MOSAiC expedition was the stack of the ship. Based on Fig. 1, it is possible to define a polluted wind sector from 90 - 270° relative to the bow of the ship. The wind-based filter flags all data points collected  
215 when the relative wind direction was coming from the polluted sector. This wind filter is introduced here for comparative purposes only. The comparison of the wind-based filtering method to the PDA is presented in Sect. 3.2.1.

### 2.3 Visual filtering method

The following visual filtering method is introduced here for comparative purposes: Every pollution filtering method contains a certain level of subjectivity since the final decision about polluted vs non-polluted must be made by the user. Therefore, we  
220 compared the performance of the PDA to the result of a visual-only filtering method, which was applied to the dataset of the CPCf. Impact from local pollution is often evident from the time series of pollution-related variables, such as wind direction, wind speed, total particle number concentration, one standard deviation of particle number concentration within one minute periods ( $N_{\text{std}_1\text{m}}$ ), and particle number size distribution. Time series of these variables were visually inspected for each day to identify the periods impacted by the local pollution.  $N_{\text{std}_1\text{m}}$  was used as the core feature of pollution influence. In periods  
225 unaffected by pollution, it was below 30 cm<sup>-3</sup>. When the total particle number concentration was higher than ~600 cm<sup>-3</sup> (such as during new particle formation events in the summertime, or during Arctic haze events in the wintertime),  $N_{\text{std}_1\text{m}}$  often increased to between 30 to 100 cm<sup>-3</sup>. However, these periods were not treated as local pollution influenced. Data were flagged as polluted when  $N_{\text{std}_1\text{m}}$  was above 10<sup>3</sup> cm<sup>-3</sup>, the Aitken mode particle (i.e. diameter below 100 nm) number concentration was greatly enhanced and wind was coming from the stack direction. Periods moderately influenced by the local pollution, during  
230 which  $N_{\text{std}_1\text{m}}$  was typically between 10<sup>2</sup> to 10<sup>3</sup> cm<sup>-3</sup> and the wind direction was usually not directly from the stack direction, are also flagged in this dataset. The visual filtering method also considered spikes and neighboring points. A spike of  $N_{\text{std}_1\text{m}}$  was defined as a point having a value that was 2 times higher than the 5-min moving average of  $N_{\text{std}_1\text{m}}$ . When two polluted flags were within 5-min of each other, all data points in between were flagged as polluted.

### 2.4 Pollution detection algorithm (PDA)

235 During MOSAiC, local pollution occasionally originated from other sources than the stack, such as helicopters, snow groomers and snowmobiles, as well as small diesel generators on the ice. Therefore, the algorithm needs to detect pollution from different sources and directions. Figure 1 shows the whole dataset of minute-averaged particle number concentrations, as a function of the relative wind direction. Note that we used this particle number concentration dataset to develop the PDA. The stack is



located at  $180^\circ$  from the bow and is marked as a grey vertical line in the figure. The majority of high concentration events  
240 ( $>10^4 \text{ cm}^{-3}$ ) are related to emissions from the stack, but there were occasions where high concentrations came from different  
directions. We define high concentrations as  $> 10^4 \text{ cm}^{-3}$  because empirically we did not find any situation where the particle  
number concentration would increase to such high values in the Arctic without involvement of expedition-related activities  
(see Sect. 2.3.1). In contrast, we find low particle number concentrations of  $< 100 \text{ cm}^{-3}$  for almost all wind directions, including  
from the stack direction. A stable and very low boundary layer occasionally avoided the polluted air from the stack to down-  
245 mix to the inlets of the *Swiss Container* so that the measurements remained unaffected by it despite the air coming directly  
from the exhaust (this is illustrated in the picture in Fig. A5). This makes it difficult to apply a simple, but commonly-used  
(Leck et al., 1996; Cox et al., 2003) filter based on wind direction. In addition, introducing a maximum concentration as a  
single threshold below which data are considered clean is not feasible, because natural particle concentrations vary across  
several orders of magnitude (Fig. 1). Pollution influence can also occasionally be so small that it would not surpass the  
250 threshold, e.g., when it is on the order of hundreds of particles on top of a low (e.g.,  $< 100 \text{ cm}^{-3}$ ) natural concentration (baseline  
concentration).

Generally, concentration data from remote regions, characterized by the absence of dominant local (anthropogenic) sources,  
vary only slowly with time, compared to when influenced by local pollution. This means that the concentration gradient (time  
derivative) is small. In contrast, concentration data show distinct variations, such as rapid fluctuations, when affected by  
255 pollution from nearby sources (e.g., Fig. A4). The PDA builds on this abrupt variation in concentration and detects polluted  
data based on the rate and magnitude of change in the concentration signal over a given time period. The basic principle of the  
PDA was developed and used for the 2018 Microbiology-Ocean-Cloud-Coupling in the High Arctic (MOCCHA) campaign  
on the Swedish ice breaker *Oden* by Baccharini (2021). Here, we further develop this algorithm and test it against different  
datasets. Importantly, the algorithm is only based on target concentration data and does not rely on ancillary datasets, such as  
260 particle size distribution or meteorological variables. This brings the advantage that the PDA is applicable to a large number  
of datasets measured in remote environments (e.g., polar observatories, continental and marine background measurement sites  
or ship expeditions).

We also provide an open source, python-based, tool for download on zenodo (<https://doi.org/10.5281/zenodo.5761101>),  
including a manual, which allows users to apply the same method to other datasets. The PDA consists of a set of filters which  
265 can be applied in various combinations to identify polluted data. Figure 2 shows a schematic of the workflow. First, data points  
with a gradient exceeding a given threshold are tagged as polluted (Sect. 2.3.1). Second, a simple threshold filter tags data  
points which exceed a specific threshold, e.g.,  $> 10^4 \text{ cm}^{-3}$  in our case because such concentrations are beyond the expected  
range for the central Arctic (see Sect 2.3.2). Optionally, for every tagged data point, the neighboring point can be tagged, too  
(Sect. 2.3.3). An optional median filter identifies outliers in the dataset which are left untagged (Sect. 2.3.4). Lastly, sparse  
270 data points left untagged in a series of tagged data points are also tagged (Sect. 2.3.5). Individual parameters and thresholds in  
each step can be adjusted to customize the PDA and to adjust its strictness. The neighboring and the statistical median filters  
are optional and can be skipped, for example if the resulting segregation of polluted data points satisfies the needs of the user



275

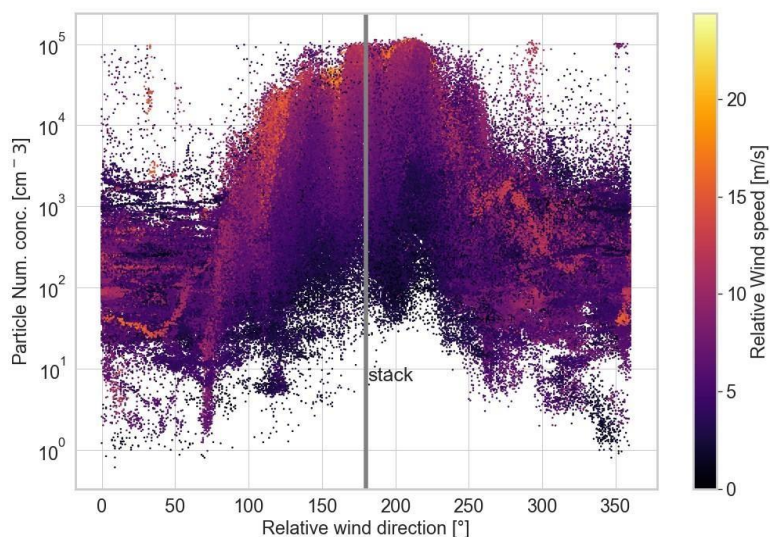
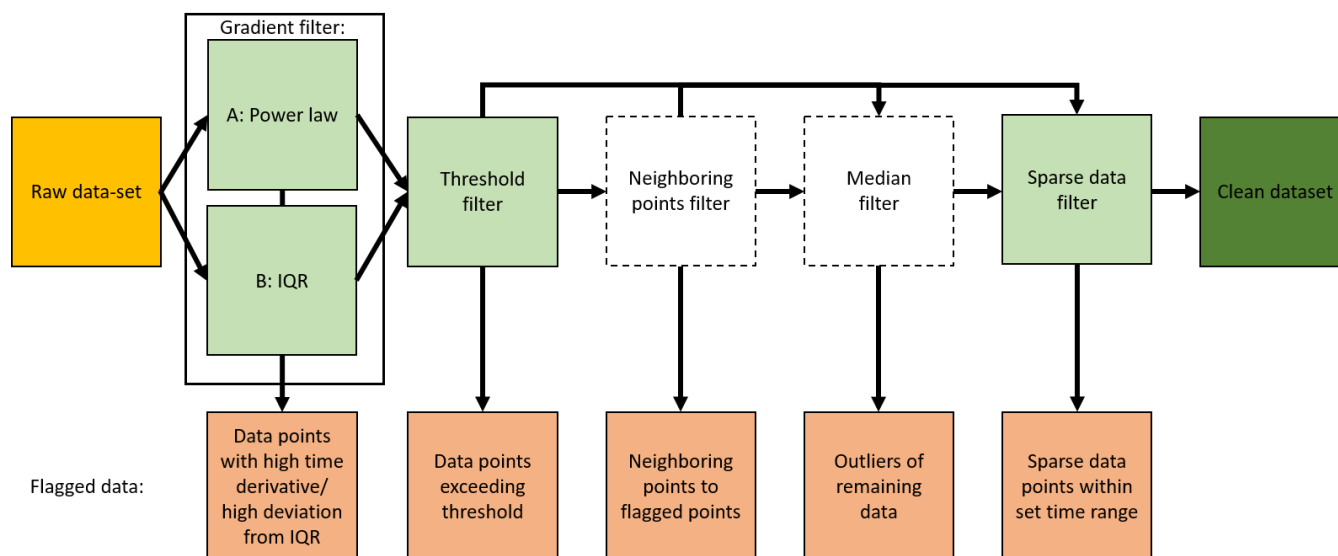


**Figure 1:** Particle number concentrations averaged over one minute as a function of relative wind direction (0° indicates wind coming from the bow) and color-coded by relative wind speed. Concentrations were higher with winds from the broader direction of the stack (located at 180° from the inlet position, this position is marked with a vertical line).

280





285 **Figure 2: Schematic of the pollution detection algorithm. The key is the gradient filter (highlighted in a black rectangle), which is followed by a series of steps. The neighboring points and the median filter (in white) are optional and can be skipped. Parameters of each step can be adjusted. Orange boxes indicate flagged data points, green and white boxes show unaffected data which are forwarded to the next step. IQR stands for interquartile range (see Sect. 2.4.1).**

### 2.4.1 Step 1: Gradient filter

290 The gradient filter is used to separate periods characterized by rapid fluctuations in concentrations (we consider them as polluted periods), from those dominated by slow changes in concentration (we consider them as unaffected periods). At each data point in the native time resolution (10 s in our dataset) we calculate the absolute value of the time derivative (i.e., the gradient over time) of the concentration.

$$\left| \left( \frac{dC}{dt} \right)_t \right| \approx \left| \frac{C_{t+\Delta t} - C_{t-\Delta t}}{2\Delta t} \right| \quad \text{Eq. (1)}$$

295 where  $\left( \frac{dC}{dt} \right)_t$  refers to the time derivative of concentration  $C$  at time  $t$ ,  $C_{t+\Delta t}$  and  $C_{t-\Delta t}$  refer to the concentration  $C$  at time  $t + \Delta t$  and  $t - \Delta t$ , respectively.  $\Delta t$  refers to the time interval between two data points. To separate polluted from unaffected data we developed two methods:

Method A separates polluted from unaffected data with a power law. We average the time derivatives of the particle number concentration over one minute and plot them against the one minute-averaged particle number concentrations (Fig. 3). The averaging time can be varied and adapted to datasets with different time resolutions. This is discussed in Sect. 3.1. We choose one minute for a pragmatic reason: At one minute time resolution we can still see influences of short-lived changes in particle number concentration (e.g., from pollution) and it makes data processing faster as the size of the one-year long dataset is large. Figure 3a shows two “branches” of data points (visually emphasized by the relative wind direction color code): One with higher gradients representing periods of high concentration variability, i.e., due to local pollution, and one with lower gradients, indicating smooth variation, i.e., not affected by local pollution. Separating the polluted and unaffected branch is the fundamental step of the PDA developed here. The time derivative of the particle number concentration can be described as a power law of the particle number concentration, and the two branches distribute around two different power laws. Thus, for the separation, we use a power law ( $y = a * x^m$ ) between those two branches ( $m$  corresponds to the slope, and  $\log(a)$  to the intercept with the logarithmic y-axis). Values for  $m$  and  $a$  have to be determined empirically to place the line between the two gradient branches. An approximate first value for  $m$  and  $a$  can be found by extracting two points  $(x_1, y_1)$  and  $(x_2, y_2)$  from the graph:

$$m = \frac{\log(y_2/y_1)}{\log(x_2/x_1)} \quad \text{Eq. (2)}$$

$$a = y_1/x_1^m$$



315

Eq. (3)

Finding optimal values for  $a$  and  $m$  is an empirical process which can be verified by looking at the time series of the polluted and unaffected data together. This process likely needs several iterations until values for  $a$  and  $m$  are found which satisfy the needs of the intended data analysis. A higher slope in the separation line means that, for a fixed particle number concentration, the threshold of separation moves towards higher gradients of particle number concentration, and therefore allows more variability in the data, i.e., the method is less strict. A higher intercept sets the threshold of separation to higher gradients at lower concentrations, allowing for more variability there. Examples of four different separation lines are shown in Fig. 3a. For the MOSAiC dataset, we found a value of  $m = 0.55 \text{ s}^{-1}$  and  $a = 0.5 \text{ cm}^{-3}\text{s}^{-1}$  (red line) to work well with our dataset (see Sect. 3.1).

Method B separates data based on the interquartile range (IQR) of the gradients within a defined period. Not all datasets show an equally clear separation of the gradients into two branches like the particle number concentration shown in Fig. 3a. An example is the particle number concentration dataset from Jungfraujoch (Fig. 3b). An alternative method is thus to separate polluted from unaffected data based on the deviation of the gradients from their IQR. For this, we calculate the IQR of the gradients of each data point in a moving window of a set duration (24h in the case study described in Sect. 3.4.4, which is equal to 1440 data points). When the absolute gradient of a data point exceeds the 75<sup>th</sup> percentile by a given factor (hereafter called IQR factor), the data point is flagged. We use an IQR factor of 1.7 to identify pollution in the JFJ dataset. Both the window size and the separation factor of the IQR method can be adjusted in the PDA code. Method B is well suited to separate datasets with less obvious difference between pollution and unaffected periods.

#### 2.4.2 Step 2: Threshold filter

For specific regions, like the central Arctic in our case, one can assume concentrations not to exceed a certain threshold as long as they are not influenced by local pollution sources. Based on the particle number concentration dataset throughout the whole MOSAiC and MOCCHA observation periods, we argue that it is safe to assume that particle number concentrations above  $10^4 \text{ cm}^{-3}$  can be considered as influenced by local pollution with the detection limits of the instruments used for the two campaigns. Note that new particle formation events, which typically lead to the highest number concentrations second to ship activities during the expedition, do not exceed this threshold. See Fig. 3, where the branch of unaffected data below the separation line does not show any data points  $> 10^4 \text{ cm}^{-3}$ . A similar principle is applied to a lower limit, here  $60 \text{ cm}^{-3}$ . Below this threshold, we assume the dataset is not influenced by pollution. This threshold helps to maintain the baseline when a sudden concentration drop (e.g., from a precipitation event) would trigger the gradient filter. We choose  $60 \text{ cm}^{-3}$  to be a suitable threshold for this dataset because we did not observe such low values during polluted time periods, except in very rare occasions, but those data points would be detected by the sparse filter (sect. 2.3.5). Both thresholds can be adjusted in the tool, because they will vary with location, the detection limit of the instrument, averaging time, and target compound. For example, a higher lower-limit threshold might be appropriate in a remote forest region, where lower particle number concentration limits



can be as high as  $500 \text{ cm}^{-3}$  (Schmale et al., 2018). If the lower threshold is set to zero, all data below the upper limit threshold are included in the filtering algorithm. The threshold filter activates automatically with the application of the gradient filter. Hereafter we also mean the threshold filter when we talk about the gradient filter.

350

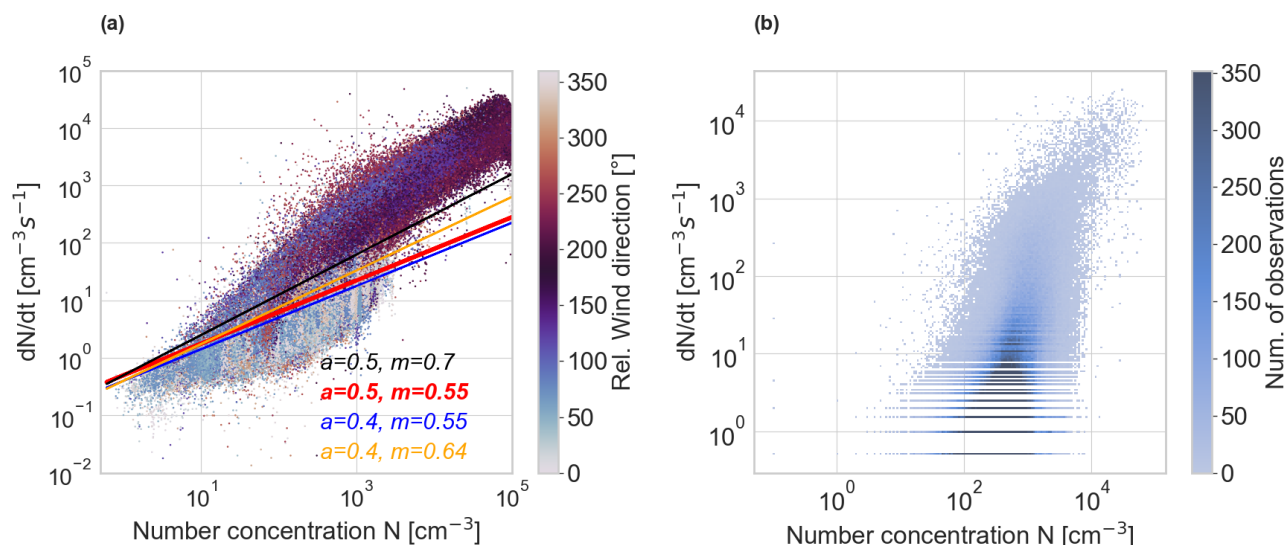


**Figure 3: Absolute value of the minute-averaged particle number concentration gradient as a function of the minute-averaged particle number concentration. A) The dataset collected during the MOSAiC expedition. The color-code indicates the relative wind direction. The four lines show potential separation lines between polluted and unaffected data points for four different combinations of slope and intercept ( $y=a*x^m$ ). Here we used the red line. B) The binned dataset collected at Jungfraujoch station in the Swiss Alps in 2016 (Bukowiecki et al., 2021). The color-code indicates the number of observations per bin.**

355

### 2.4.3 Step 3: Neighboring points filter

It can be useful to discard points at the beginning and end of polluted periods where single data points might not be tagged because the deviation of their values from previous or subsequent points is too small to be detected by the PDA. This filter targets data points at the transition from polluted to unaffected periods and vice-versa. Applying this filter is optional as it discards additional data, but in return results in a dataset less affected by local pollution. We show and discuss the results of this step in Sect. 3.1.

360

### 2.4.4 Step 4: Median filter

Here, we define individual data points that exceed a defined factor above the running median as outliers. To detect such outliers, an additional filter, based on the running median of the concentration over a time interval (hereafter called median time interval), can be applied. For each data point, we calculate its deviation from the running median over the median time interval. If the deviation exceeds a given factor above this median, it is flagged as pollution. The factor can be adjusted to

365



370 lower (stricter) or higher (less strict) values with the trade-off of more false positive data points (i.e., unaffected data points  
 flagged as polluted) or false negative data points (i.e., polluted data points which are not flagged), respectively. We found an  
 empirical deviation factor of 1.4 to support the detection of outliers for MOSAiC and keep the number of false positively  
 detected data points as small as possible. This is further discussed in Sect. 3.1.

#### 2.4.5 Step 5: Sparse data filter

375 As a last step, we apply a sparse data filter to tag leftover unaffected data points in periods affected by local pollution. More  
 quantitatively, if the sum of polluted data points in a given time window (subsequently called sparse window) exceeds a given  
 threshold (termed sparse threshold), all points in the sparse window are flagged as polluted. We use a sparse threshold of 24  
 within 30 data points (which corresponds to 30 minutes in our case). The sparse threshold and the associated time-window can  
 be adjusted in the PDA. The sparse data filter is automatically activated as the final filtering step. To de-activate the sparse  
 data filter, one can simply set the sparse threshold to the same number of data points as in the sparse window.

380

**Table 1: Overview of all filter steps and parameters of the PDA applied to different datasets.**

Filter step	Parameter	Particle number concentration MOSAiC	Particle size distribution MOSAiC	CO <sub>2</sub> MOSAiC dataset	Particle number concentration JFJ	Particle number concentration CPCf
<b>1A. Gradient filter (Power law)</b>	a m	0.5 cm <sup>-3</sup> s <sup>-1</sup> 0.55 s <sup>-1</sup>	1.4 cm <sup>-3</sup> s <sup>-1</sup> 0.5 s <sup>-1</sup>	- -	- -	0.5 cm <sup>-3</sup> s <sup>-1</sup> 0.5 s <sup>-1</sup>
<b>1B. Gradient filter (IQR)</b>	IQR factor IQR window size	- -	- -	1.5 24 h	1.7 24 h	- -
<b>2. Threshold filter</b>	Upper threshold Lower threshold	10 <sup>4</sup> cm <sup>-3</sup> 60 cm <sup>-3</sup>	10 <sup>4</sup> cm <sup>-3</sup> 60 cm <sup>-3</sup>	none none	10 <sup>4</sup> cm <sup>-3</sup> 60 cm <sup>-3</sup>	10 <sup>4</sup> cm <sup>-3</sup> 60 cm <sup>-3</sup>
<b>3. Neighboring points filter</b>	On/off	On	On	On	On	On
<b>4. Median filter</b>	Median time interval	30 min 1.4	30 min 1.4	30 min 1.001	30 min 1.5	30 min 1.3



	Median deviation factor					
<b>5. Sparse data filter (no. of data points)</b>	Sparse window	30	10	30	30	30
	Sparse threshold	24	3	20	24	23

### 3 Results and discussion

In this section, we present and discuss the performance of the PDA and compare the results to other commonly used approaches to identify local pollution (wind direction and visual inspection methods). We test the PDA on different types of atmospheric measurements as well as on particle number concentration datasets with different time resolutions.

#### 3.1 Performance of the PDA

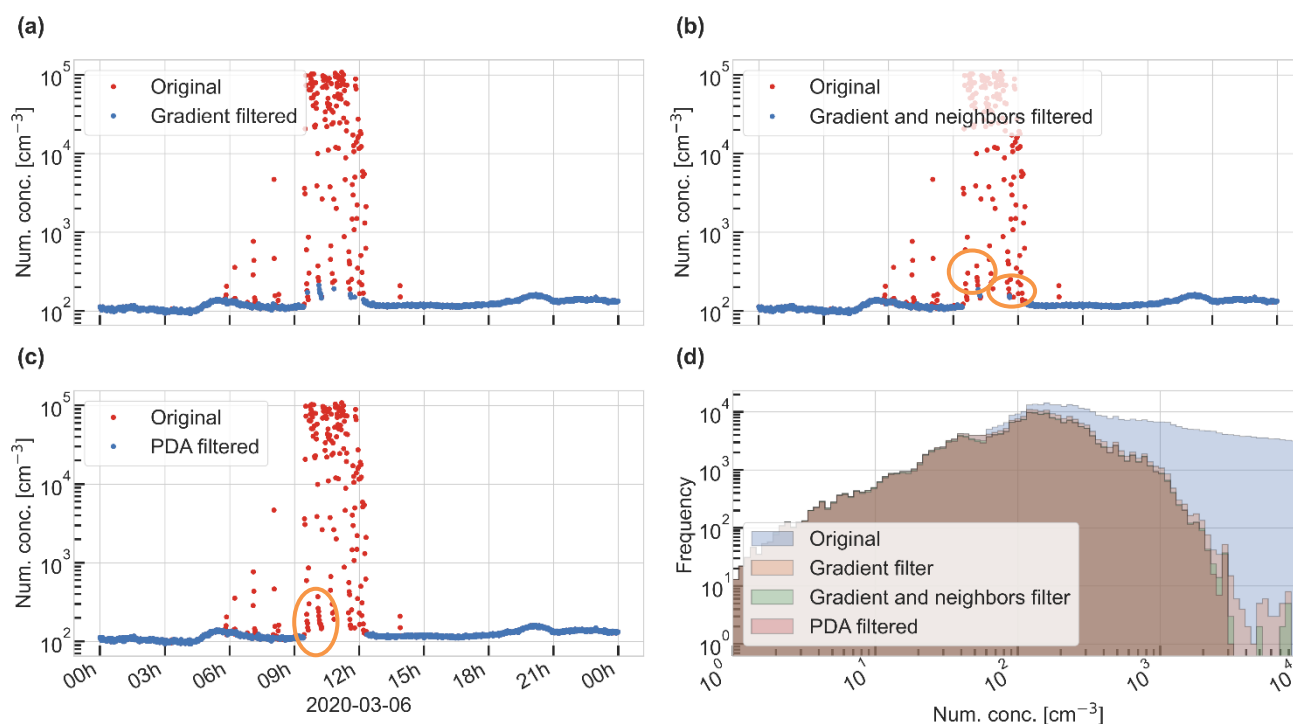
First, we demonstrate the effect of the successive application of the various pollution filter steps, and second, we evaluate the performance of the final PDA settings against characteristic situations from the MOSAiC expedition. While the algorithm was applied to the entire dataset, below we show 24-hour case studies to illustrate the results.

Figure 4a-c shows, for the case study from March 6, 2020, how the individual filtering steps (the gradient filter, the gradient filter combined with the neighboring points filter and all filters together) affect the final cleaned particle number concentration dataset. The original time series is marked in red, while the cleaned dataset appears in blue. The case study shows a stable signal with concentrations around  $100 \text{ cm}^{-3}$ , which is interrupted by a pollution event with particle number concentrations up to  $10^5 \text{ cm}^{-3}$  from 09:00 to 12:00 UTC. The gradient filter (Fig. 4a) detects the majority of the polluted data points. Only 10 data points in this period remain untagged. Including the neighboring points filter (Fig. 4b) and the median and sparse data filters (Fig. 4c), removes all those points, improving the performance of the algorithm. Figure 4d shows histograms of the entire MOSAiC particle number concentration record for the original dataset, and after application of the gradient filter, the gradient and neighboring points filter and all filters. Concentrations below  $200 \text{ cm}^{-3}$  remain nearly untouched by all filters in the PDA. The strongest filter effect is visible at larger number concentrations ( $> 3000 \text{ cm}^{-3}$ ), where only a few counts remain in the cleaned dataset. In accordance with the threshold filter, number concentrations above  $10^4 \text{ cm}^{-3}$  are removed. The application of all the filters combined is not always necessary, as shown in Fig. A6. Here, the gradient filter already detects all the polluted data points and no further filters are needed. This allows retaining more data for further analysis than when all filters are applied. Table 2 shows how the year-round dataset is reduced in size after applying the gradient filter, the gradient and neighboring points filters, or all filters combined. The second row shows the percentage of the original dataset that is left after applying the respective filters. After application of the gradient (and threshold) filter, 44 % of the data points are retained,



showing the importance of the application of a filtering method in general. Applying further filtering with the neighboring points and median filters removes only 5 % and 1 % of additional data points, respectively. This demonstrates that the gradient filter alone captures the majority of locally polluted data points (90 %), while the additional filters have a “fine tuning” effect. This effect can still be very important for individual cases as shown in Fig. 4a-c. Figure A7 summarizes the percentage of clean data per day after application of the PDA for the whole expedition. The data were most affected from pollution in spring and summer and least affected in winter. Note, this graph is indicative of pollution visible in the particle number concentration data and not necessarily for all atmospheric chemical and microphysical measurements taken during MOSAiC.

415



**Figure 4: Comparison of the gradient filtering method with additional filtering steps. Cleaned data (in blue) are plotted over raw data (in red). a: only gradient filter applied. b: gradient and neighboring points filters applied. c: all filters applied. d: Histogram of the remaining datasets after steps b) and c). “PDA filtered” means all options of the PDA were applied. For all plots we used data from the CPC3025. Raw data have only been pre-cleaned for zero filter measurements. The orange circles indicate areas where the additional filters remove additional data points.**

**Table 2: Number of data points and percentage (relative to raw data) of data left when different filtering steps are applied. The wind filter results are shown for comparison.**

425



	Original data, no filter	Gradient filter	Gradient and neighboring points filter	All filters applied	Wind filter
Dataset size	521593	231269	204077	196628	213748
Percentage	100	44	39	38	41

### 3.1.1 Case studies

Particle number concentrations in the Arctic can vary by orders of magnitude. To verify that the algorithm can be used in different environmental and pollution conditions, we tested its performance in characteristic situations throughout the expedition.

First, in conditions when the dataset is not affected by strong pollution spikes, it is required that the algorithm still detects small influences from local pollution. Figure 5a shows a day in January with a very stable and low boundary layer, resulting in a stable particle number concentration baseline around  $150 \text{ cm}^{-3}$  and occasional pollution spikes around noon. The algorithm successfully detects polluted data points and leaves the baseline untouched. In contrast, the wind filter would not detect any of the pollution. In this case, a stricter wind filter would not be possible since it would basically have to be extended to all wind directions. Second, under very polluted conditions, the requirement for the algorithm is to detect the full pollution period and to not leave polluted data points undetected (false negatives).

In Fig. 5b, a transition from unaffected to polluted conditions can be seen around 09:00 UTC due to changes in wind direction that resulted in stack exhaust contamination. The variability in the signal increases strongly and so does the gradient between data points. The PDA detects all relevant points as pollution. The wind filter would, in this case, also detect all the relevant points, but would become effective much earlier and thus detect false positives.

Third, new particle formation (NPF) and subsequent growth of particles is a common process in the Arctic which leads to an increase in particle number concentrations over a relatively short time (Kulmala et al., 2014; Baccarini et al., 2020; Schmale and Baccarini, 2021; Beck et al., 2021). This could potentially cause the gradient algorithm to accidentally flag naturally high concentrations as pollution (false positives). We analyze one NPF event observed on June 21, 2020 where the particle number concentration increased from  $< 100 \text{ cm}^{-3}$  to more than  $1000 \text{ cm}^{-3}$  within 3 hours (Fig. 5c). In addition, a few pollution spikes were observed during the NPF event. The gradient filter detects the pollution spikes and leaves the baseline untouched during the NPF-driven rise as well as during the subsequent drop in particle number concentration later in the day. If a specific case study on this NPF event was done, the user could decide to apply the PDA only to this event and tune the parameters specifically. Here we show that the settings chosen for the entire campaign treat the NPF event adequately.

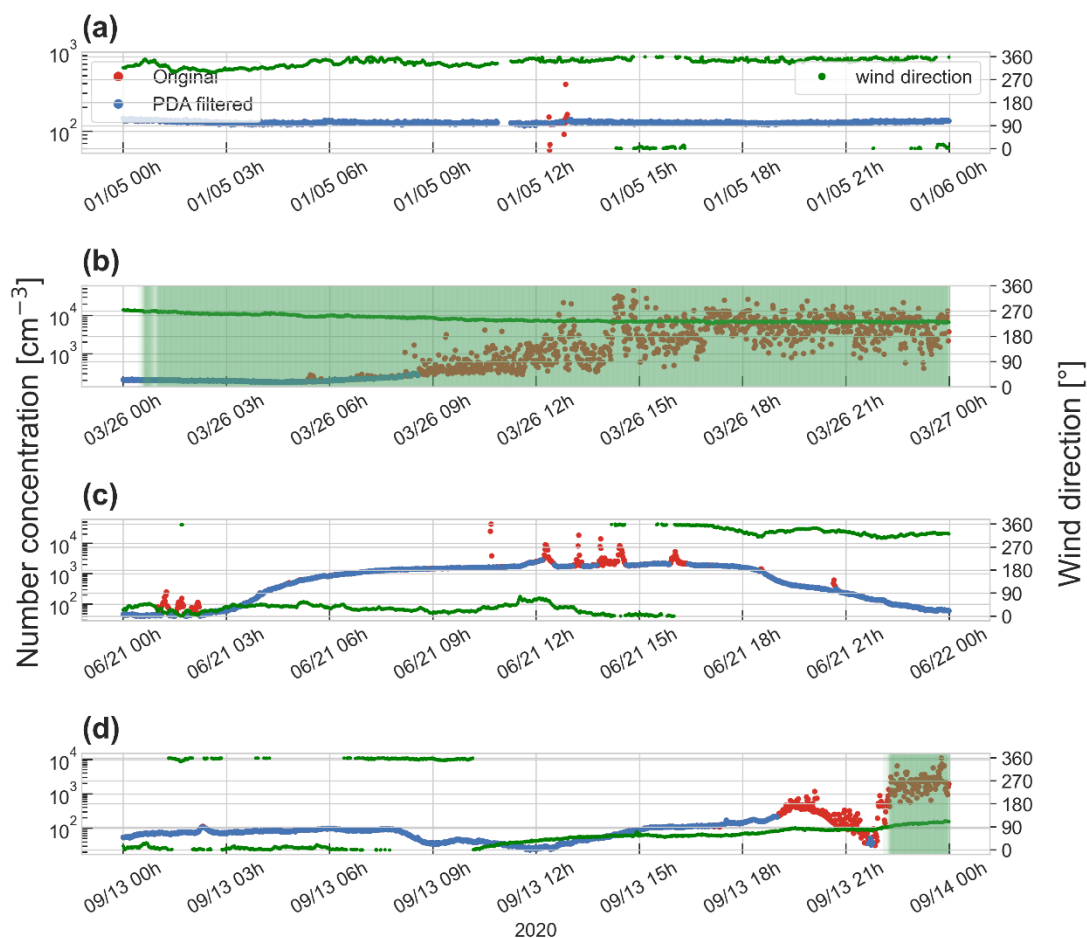
Fourth, another potentially challenging situation for the algorithm are wet-removal events. Aerosols can be washed-out of the atmosphere by rain or snow and their number concentration can decrease fast, leading to elevated gradients. We report such event observed on September 13, 2020 from 09:00 to 12:00 (Fig. 5d). The rate of change of the particle number concentration



455 is not strong enough to cause false positives. These results demonstrate that the algorithm is able to deal with relevant situations  
and is therefore an adequate tool to clean particle number concentration datasets, which are influenced by both natural  
variability and local pollution sources.

To verify that the spikes in particle number concentration can be assumed to be caused by pollution and not by a natural local  
(or regional) event, we compare the particle number concentration data during a pollution event with several other signals like  
nitric oxide (NO), CO and BC (Fig. A4). The main pollution spike in this example (ca. 18:00) coincides with the NO signal,  
460 which also shows a distinct spike at the same time (panel a). The BC signal also reacts during this event with elevated  
concentrations (panel d). The CO signal does not react at this time. This is in agreement with what we observed during the  
expedition and highlights the issues in operating the automated purge system in the AOS container (Sect. 2.1). The ship exhaust  
from RV *Polarstern* during the MOSAiC expedition did not consistently show elevated CO signals that could allow CO to be  
used to identify pollution reliably. However, there were cases where apparent pollution events did result in higher observed  
465 CO concentrations. During the event described here, there are two minor spikes at 08:00 and 10:00 where the particle number  
concentration shows spikes that coincide with the CO signal (panel b). In contrast to the first example at 18:00, the wind  
direction was not coming from the stack. This points towards a different local source of pollution, e.g., a skidoo, snow groomer  
or ship vent. These indicators let us conclude that the particle number concentration signal is sensitive to pollution from  
different sources and therefore provides a good base for the development of the PDA.

470



475

**Figure 5: Performance test of the PDA method in four different situations. a) Under overall stable conditions, b) Transition from clean to polluted conditions, c) A natural increase in particle number concentration due to new particle formation, and d) A natural decrease in particle number concentration due to a precipitation event (freezing rain) in the morning (from 9 to 12 UTC). Green shaded areas indicate where the wind filter would flag data as polluted. Green points show the wind direction, red points show the raw particle number concentration, overlaid with the cleaned data points in blue.**

### 3.1.2 Application of the PDA to particle size distribution

We applied the PDA with the parameters given in Table 1 to the measured total particle number concentration time series (i.e., the sum of the concentration of all size bins) of an SMPS dataset, collected during the MOSAiC expedition in the *Swiss Container*. The result is shown in Fig. 6 on a seven days subset of the particle size distribution (PSD) dataset. The polluted periods are clearly visible in the PSD and show as distinct yellow vertical lines. At the same time, the total number concentration shows strong spikes. The PDA detects the polluted periods (shown as red data points) and leaves unaffected data (shown as black data points). This validates the functionality of the PDA. The SMPS data have a time resolution of three

480



485 minutes, which shows the ability of the PDA to detect pollution in datasets with different time resolutions. More tests of the PDA with datasets of different time resolutions are discussed in appendix B.

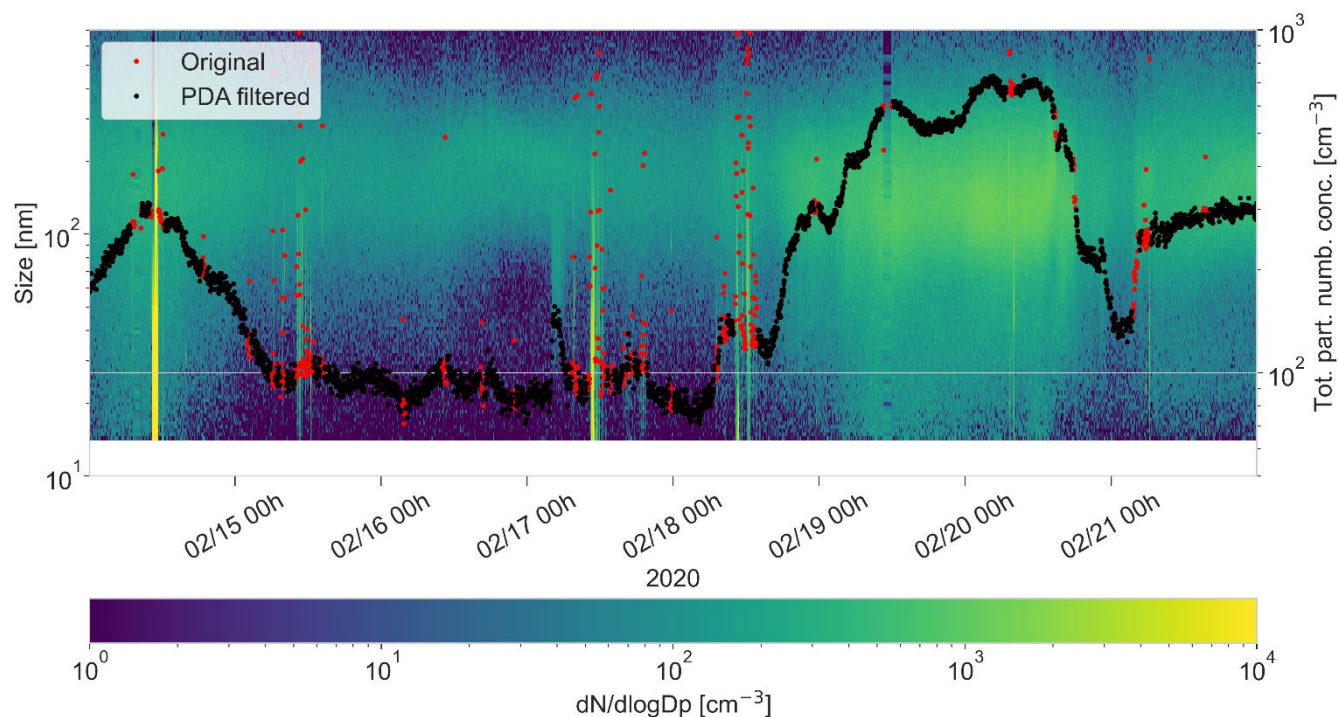


**Figure 6:** Application of the PDA to the total number concentration dataset (black line) collected by an SMPS. Data points identified as polluted by the PDA are marked in red. The dataset is plotted over the particle size distribution data of the same instrument.

490

### 3.2 Comparison of the PDA to other commonly-used methods

#### 3.2.1 Comparison to the wind filter

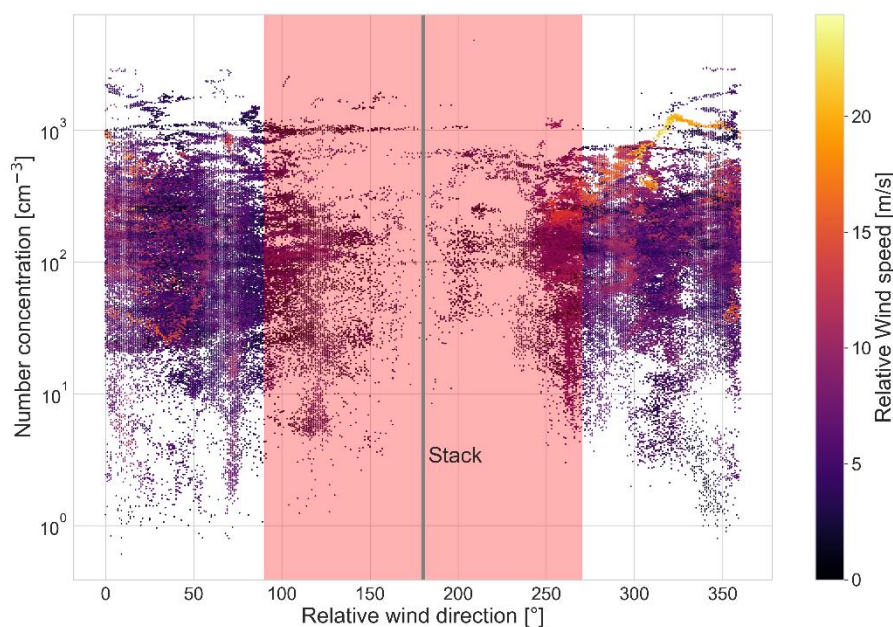
The majority of pollution events is associated with wind arriving from the direction of the stack of the ship (Fig. 1). Thus, applying a simple filter based on wind direction might be sufficient to discard most polluted data. An example is shown in Fig. 7 where we assumed a polluted wind sector between 90° and 270° and marked all tagged data points with a red band. The wind filter flags 59 % of the data as polluted. However, apart from detecting a large portion of polluted data, it also creates false positives, i.e., it flags unaffected data as polluted, as described in Sect. 3.1. It also does not detect any polluted data outside of the polluted wind sector. This is illustrated in Fig. 8 for the 17<sup>th</sup> of February, 2020, where we compare the wind filter (panel b) with the PDA (panel a). On that day, the wind came from the port side of the ship and carried polluted air from a snow groomer. The PDA (panel a) detects and tags all polluted data, whereas the wind filter does not (panel b). In addition, the PDA allows keeping unaffected data in the polluted wind sector (Fig.7). The wind direction method might, however, be simple and easy to clean data when the only source of local pollution is a point-source, and if the only pollution source is in a

500

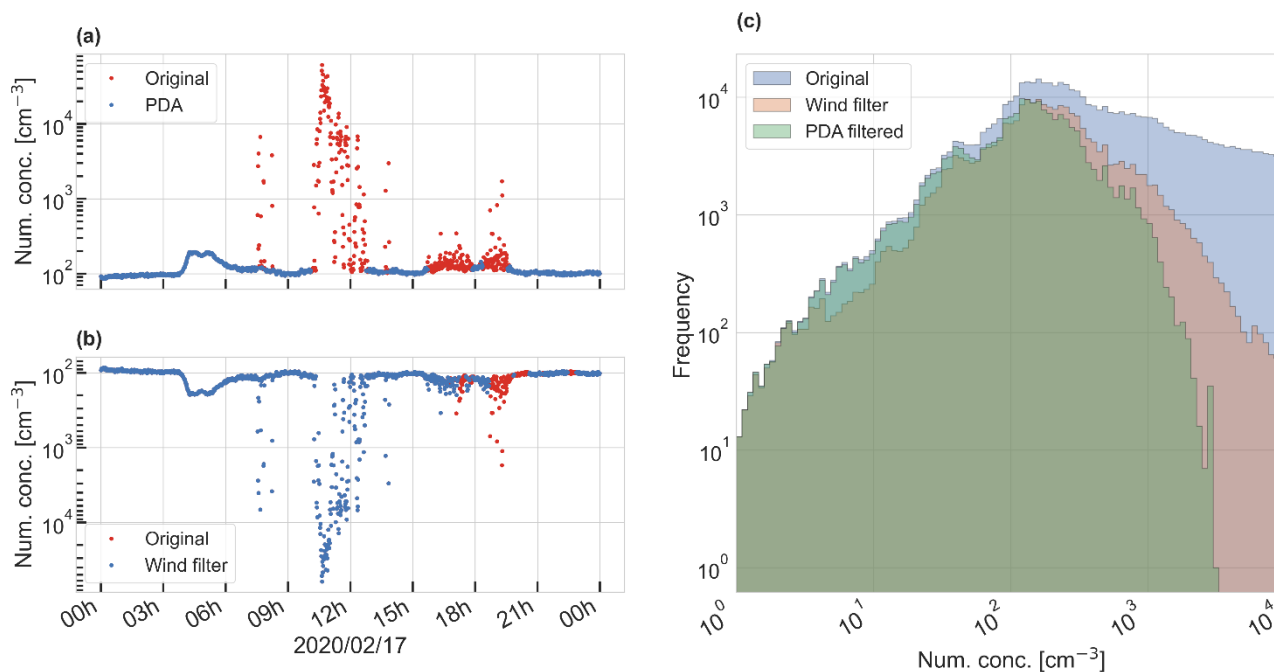


fixed wind direction from the measurement point. Although widely used on ship campaigns (see Sect. 1), the wind filter is not well suited for those campaigns, where multiple and moving emission sources exist.

505



510 **Figure 7:** Same as Fig.1 but after applying the PDA to the dataset. Flagged data points were removed to visualize the data product after application of all filtering steps. The red shaded area indicates where the wind filter would flag polluted data (between 90° and 270° relative to the bow). The direction of the stack is marked at 180° as a vertical line.



515 **Figure 8: Comparison of the PDA (a) with the wind-based method, assuming a polluted-air sector of 90° to 270° from the bow (b, mirrored). Both filtered time series (blue) are overlaid with the original raw data (red). The wind-based filter method is not case-sensitive and thus cannot detect pollution events coming from other directions than the given wind sector. Panel (c) shows histograms of particle number concentrations before (blue) and after application of the PDA (green) and the wind mask (red).**

### 3.2.2 Comparison of the PDA to the visual inspection method

We applied the PDA to a dataset independently cleaned by visual inspection and compared the results of these two methods. The dataset used for this test was collected from the ARM AOS container during the MOSAiC expedition. The visual filtering method is described in Sect. 2.3. The parameters used to apply the PDA to the dataset are listed in Tab. 1.

520 Both methods detect roughly the same fraction of clean data and agree in 93.9 % of all data points (see Table 3). The visual filtering method identifies slightly more clean data. Figure 9 shows the results of both methods in histograms. It shows the distribution of the raw data points (in grey) and the fraction of data points where the two methods do not agree, i.e., the fraction of data points which are identified as clean by the visual inspection but not by the PDA and vice versa.

525 The fact that the visual method keeps slightly more data points unaffected at lower concentrations compared to the PDA could be an indication that visual inspection detects slightly less false positives (unaffected data points detected as polluted). However, the advantage of the PDA is that it can be applied to other datasets with relatively little effort. Also, it applies strict thresholds to the dataset, which makes the result reproducible, while the visual filtering method depends on the users and their experience which makes it more prone to user bias. A comparison of both filtering methods in a time series is shown in Fig.

530 A8.



**Table 3: Fraction of clean data points of the gradient filtering method and the visual filtering method compared to the total number of data points (total counts) in numbers and in percent of the total counts.**

	Total counts	PDA clean	Visual inspection clean	Both clean	Both polluted
Data points	308750	197696	214540	196719	93233
Percentage	100	64.0	69.5	63.7	30.2

535

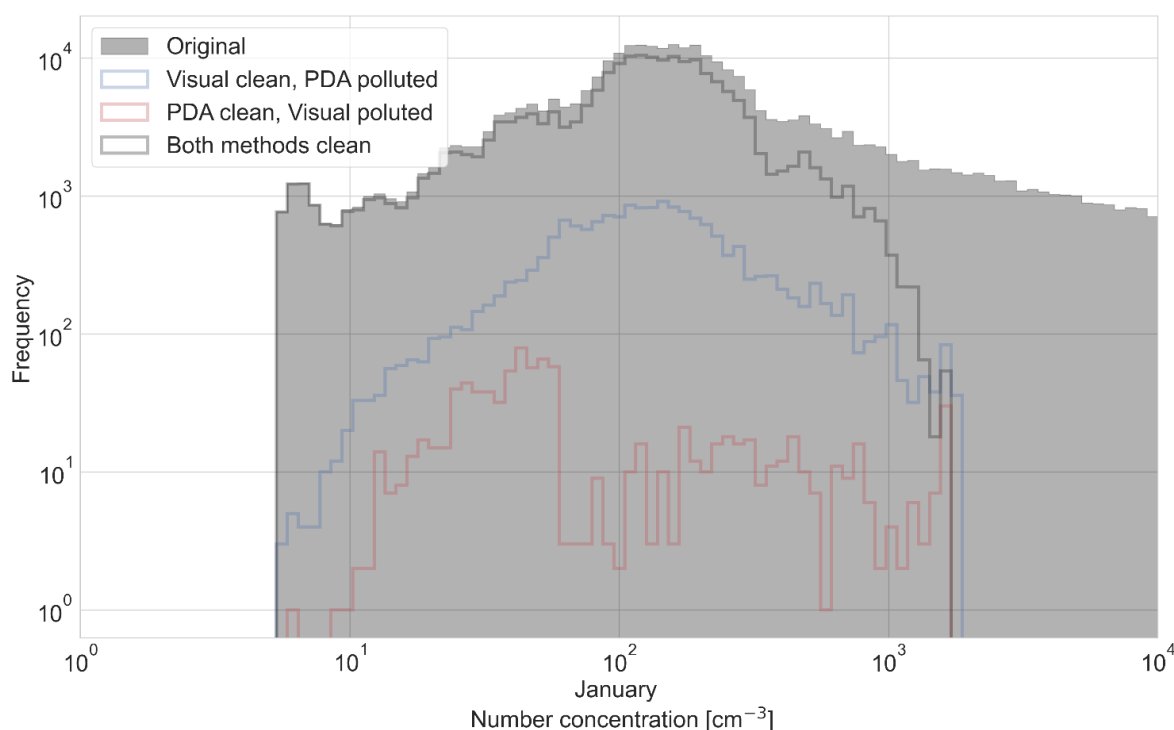


**Figure 9: Comparison of the visual inspection method to the PDA on the dataset of the CPCf of ARM. Original data are shown in grey. The blue contour line shows the fraction of data points where only the visual inspection method, but not the PDA, considered data to be clean (6 %). The red contour line shows the opposite, i.e., the data fraction of data points where only the PDA, but not the visual inspection method, considered data to be clean (<1 %). The dark grey contour line shows the fraction of data points where both methods considered data to be clean (~64 %).**

540

### 3.3 Broader application of the PDA

We test the performance of the PDA on datasets with different characteristics using time series of particle chemical composition and ambient air CO<sub>2</sub> concentrations collected during MOSAiC (see Sect. 3.4.1 and 3.4.2, respectively) and on a  
 545 particle number concentration dataset collected at JFJ in the Swiss Alps (Sect. 3.4.3).

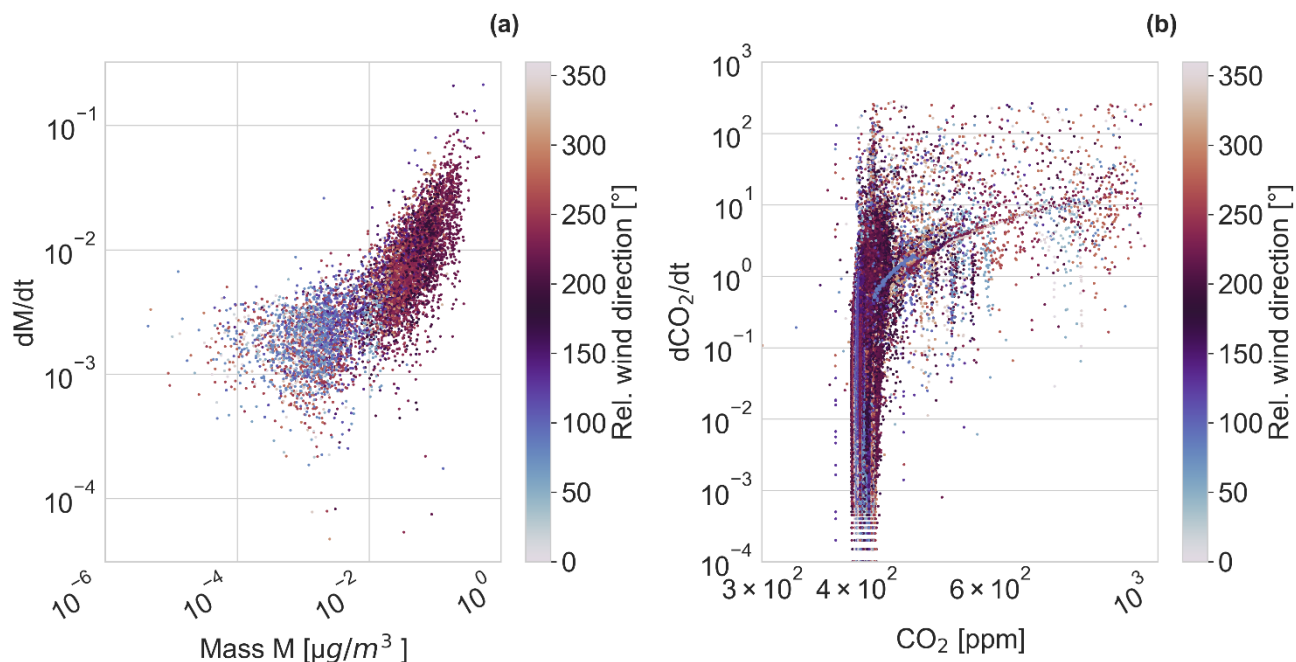


### 3.3.1 Application to aerosol chemical composition datasets

To check whether the algorithm works on other datasets than particle number concentration data, we applied it to the ion fragment signal of  $C_4H_9^+$  ( $m/z = 57$ ) measured by the AMS, which characterizes fresh pollution from combustion. In a perfect scenario, our developed algorithm is able to group the signal of this fragment ( $C_4H_9^+$ ) into high mass (and high gradient) resulting from ship emissions in comparison to low background mass concentration (and low gradient), the latter associated with a relative wind direction away from the stack ( $90^\circ$  to  $270^\circ$  relative to the bow). Figure 10a shows the relation of the gradient of the mass concentration of  $C_4H_9^+$  (averaged over 5 minutes) as a function of its mass concentration. We observe a separation of the gradients into two branches with two different slopes as in Fig. 3a. However, the mass concentrations do not overlap in the two branches of the gradients ( $dM/dt$ ) of clean and polluted periods, therefore a separation based on the gradient is impossible. This is also visible based on the wind direction (indicated by the color); a separation between the ‘pollution’ and ‘clean’ data points occurs at approximately  $10^{-2} \mu\text{g}/\text{m}^3$ , resulting in a critical concentration threshold rather than a defined slope. However, such a separation at a defined mass concentration grouped certain ‘clean’ data points into the ‘polluted’ category and thereby failed to produce a reliable pollution mask. Our hypothesis for the failure of the gradient algorithm when applied to AMS data is that the AMS has a lower particle cut-off of 70 nm and the  $> 70$  nm particles detected by the AMS are affected by pollution in a different way than the entire particle population also containing smaller particles, as reflected by the CPC data, which contains particles as small as 3 nm. We found the typical peak diameter of ship pollution observed on RV *Polarstern* was approximately 30 nm. An alternative way to produce a pollution tag for AMS data is to apply a chemically resolved method, where the mass spectrum as a whole is compared to a previously defined chemical pollution spectrum. This method is described in more detail in Dada et al. (in prep.).

### 3.3.2 Application to trace gas datasets

Figure 10b shows the distribution of the gradients for the  $\text{CO}_2$  dataset. We used  $\text{CO}_2$  data in a 1 s time resolution and averaged the gradient over 1 minute. The  $\text{CO}_2$  signal varies by less than one order of magnitude when affected by pollution. The majority of the data points do not deviate from the observed atmospheric background concentration around 400 parts per million (ppm). The color-coded wind direction also gives no indication of separation of the data by wind direction. One reason is that the magnitude of the gradient of the  $\text{CO}_2$  signal in case of pollution is low compared to its relatively high background concentration, and therefore, polluted data points do not separate clearly from the main “branch” of data points. Therefore, the separation of polluted and unaffected data points based on two branches of gradients (step 1A) does not work for the  $\text{CO}_2$  dataset. We thus applied the PDA with step 1B to the  $\text{CO}_2$  dataset. The parameters used for the PDA are shown in Table 1. An example of the resulting time series is shown in Fig. A9 on the same case study on July 27 as we described in Sect. 3.1.1. The  $\text{CO}_2$  signal is noisy and shows a strong spike between 16:00 and 20:00. This spike matches the observations described in Fig. A4. The PDA detects and flags data points within the spike as polluted. Situations like this example with a noisy signal are further discussed in Sect. 3.5. Angot et. al. (in prep.) applied this method and describe the  $\text{CO}_2$  dataset in more detail.



580

**Figure 10:** (a) Time derivative of the ion mass signal of  $C_4H_9$  ( $m/z=57$ ) compared to its total mass concentration, measured by the Aerosol Mass Spectrometer. (b) Time derivative of the  $CO_2$  concentration signal compared to its concentration, measured by cavity ring-down spectroscopy. Colors indicate the relative wind direction.

### 3.3.3 Application of the PDA to a long-term high-altitude site monitoring dataset

585 We applied the PDA to a particle number concentration dataset collected at the high-altitude research station JFJ in the Swiss Alps. The data has a time resolution of 1 minute. The calculated gradients show a very different pattern compared to those from the MOSAiC expedition (Fig. 3a,b). The difference in magnitude between pollution and the JFJ background dataset is much smaller (Fig. A10) compared to MOSAiC. The JFJ dataset is therefore well suited for separating polluted data using the IQR filtering method (step 1B). The parameters used in the PDA are shown in Table 1. The PDA was applied to an example  
590 time series from two days in July 2016 (Fig. A10), where a diurnal cycle of the baseline and pollution spikes during daytime are visible. This example demonstrates how the baseline is distinguished from the spikes even when the baseline varies by an order of magnitude. Given the different approach by Bukowiecki et al. (2021), i.e. detecting and counting spikes versus masking polluted time periods with the PDA, we cannot make a direct comparison between the two methods like in Sect. 3.2.2 (visual method). The final decision about flagging individual data points remains the user's responsibility and will depend on  
595 the objective of the analysis.



### 3.4 Limitations of the PDA

This study shows that the PDA is capable of cleaning pollution from a variety of particle and trace gas datasets. However, a challenge for the algorithm remains to deal with false negatives, which are left after applying the gradient filter (step 1 of the PDA). In situations with small pollution peaks, which occur on top of a clean baseline, this is often the case at the beginning and at the end of the affected period. The application of the neighboring points filter on top of the gradient filter improves the result significantly, but might not catch all pollution-affected points. An example of this is shown in Fig. A11a and b.

Another challenge for the PDA is situations where the signal is influenced by subtle pollution, which does not result in large spikes but rather in a very noisy signal with low amplitude above a baseline. Two examples are shown in Fig. A9 and A11. These situations are also difficult to assess for an expert using the visual inspection method. The boundary between polluted and unaffected data is blurred, and the gradient filter in Fig. A11 only flags a subset of data points that protrude from the main signal. The application of a strict PDA with all filters included could avoid false negatives. However, this might also remove unaffected data points, and it is up to the user to make this decision.

The applicability of the PDA to a dataset also depends on the response time of the instrument. A response time which is slower than the occurrence of pollution (i.e. the instrument cannot capture the sharp rise and fall in concentrations) leads to smaller gradients of the measured particle number concentrations. This would set an upper limit to the measured gradient. Still, pollution could be detected as long as this upper limit is substantially higher than the gradients of the natural signal. This does not matter for the measurements with the CPCs, since the response time is typically lower than 1 second (Enroth et al., 2018). In essence, this issue is similar to recording data in coarse time resolution, which would smear out the difference in magnitude between baseline and pollution (see Appendix B).

615

### 4. Conclusions

We developed a pollution detection algorithm (PDA) to identify periods of local pollution in atmospheric aerosol and trace gas concentration time series. The PDA was successfully tested with particle number concentration datasets from two different sites - a ship-based expedition in the high Arctic Ocean and a background station in the Swiss alps affected by tourism - as well as with a CO<sub>2</sub> concentration dataset from the high Arctic. In comparison to the commonly used wind direction method to clean datasets, the PDA is capable of identifying pollution from different sources and directions and reduces false positive and false negative results. Compared to a visual filtering method the PDA identifies a similar amount of pollution (41 % with the visual method compared to 43 % with the PDA). The PDA only uses the target concentration data and does not rely on ancillary datasets to identify polluted data points. It works for datasets with a relatively low baseline where pollution spikes exceed the baseline significantly and the sampling rate is fast enough so that the gradient of polluted signals separates clearly from that of unaffected. “Fast enough” depends on the variability of the baseline and occurrence of pollution. In our case the methods worked for time resolutions between 10 seconds and 10 min. The PDA is primarily designed for remote locations, but it might

625



also be applied to locations where local pollution interference is so frequent that the majority of data points exceeds the contribution from the underlying baseline in the period of interest, like in urban areas for example.

630 The relative magnitude of interference from local pollution varies between different measurement campaigns and may depend on the type of instrument. The PDA is best suited to identify primary pollution, i.e., for particle number concentration, or trace gases directly emitted by the pollution source (e.g., CO<sub>2</sub>), or size distribution datasets with a clear primary pollution mode. For other variables, such as for accumulation mode particle chemical composition data, which are not representative of the main pollution size range (around 30 nm), a different approach might be better (e.g., Dada et al., in prep.) because the PDA will

635 discard too many data points.

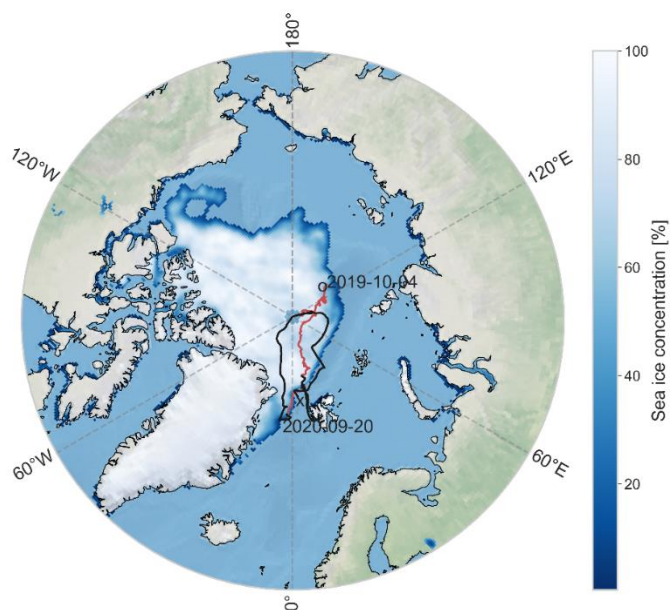
The PDA is published open-source in a user-friendly code toolkit downloadable from zenodo (<https://doi.org/10.5281/zenodo.5761101>). All PDA parameters can be adjusted to adapt it to specific datasets or to customize the filtering level for specific needs. This makes it flexible and allows its application to locations where no ancillary datasets might be available. It also allows a fast application to multiple datasets and provides an objective, reproducible method to

640 identify local pollution in remote or background conditions.



## Appendix A

645



650

**Figure A1:** Track of RV *Polarstern* during the MOSAiC expedition in the central Arctic (Schmithuesen, 2021a, c, d, e, b). Drift (red line) started in October 2019 and ended in September 2020. The black lines show periods where the ship was on transit. The sea ice extent is displayed from September 2019 at the annual minimum. We used sea ice data from the National Snow and Ice Data Center (Maslanik and Stroeve, 1999). The background map is made with Natural Earth (<https://www.naturalearthdata.com/>).

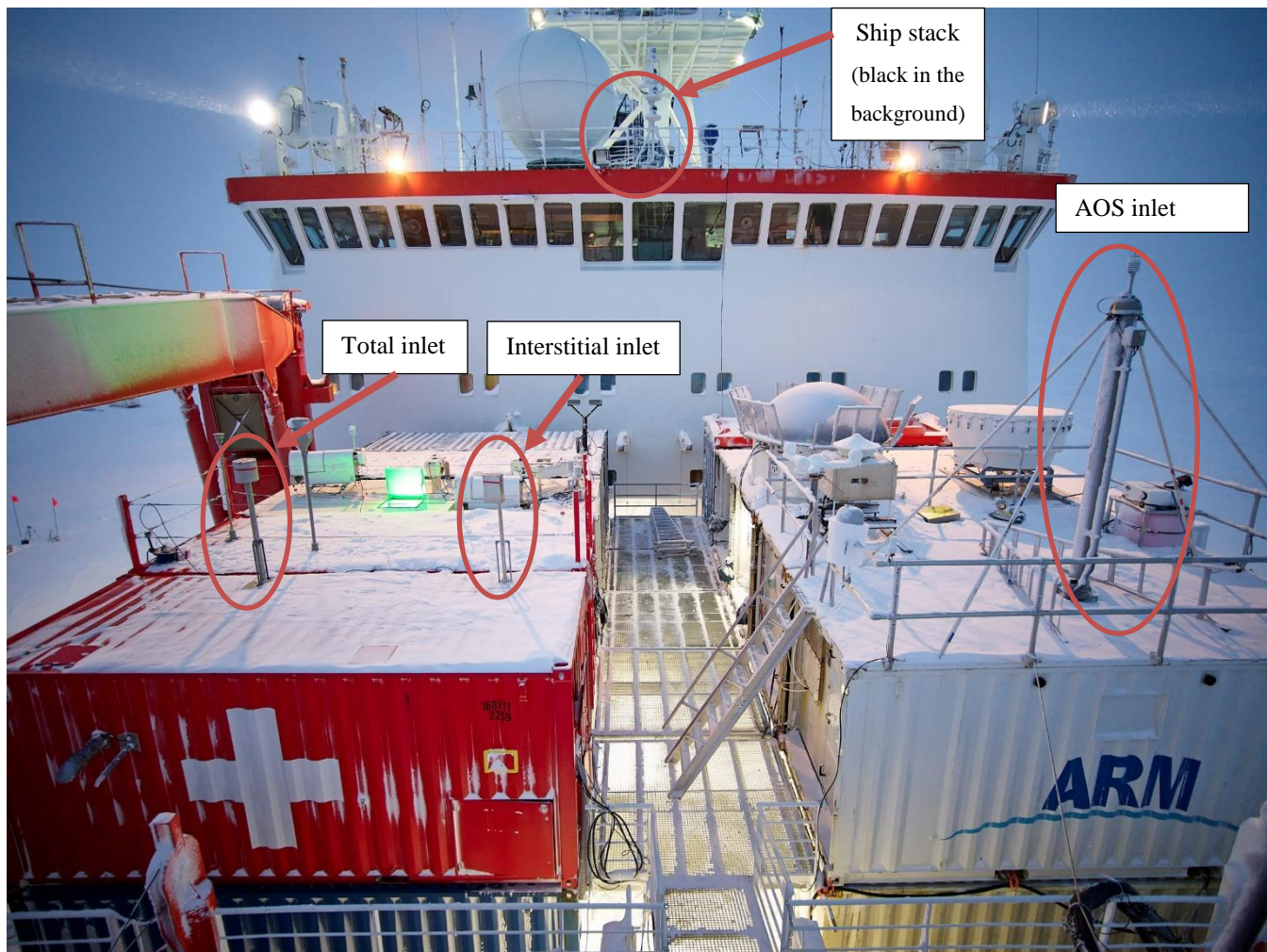


Figure A2: Bow of the ship during the expedition. In red with a white cross, the *Swiss Container* with its two inlets. The ARM measurements were performed on the port side of the ship in the white container at the front with a higher inlet. Photo credit: Michael Gutsche

655

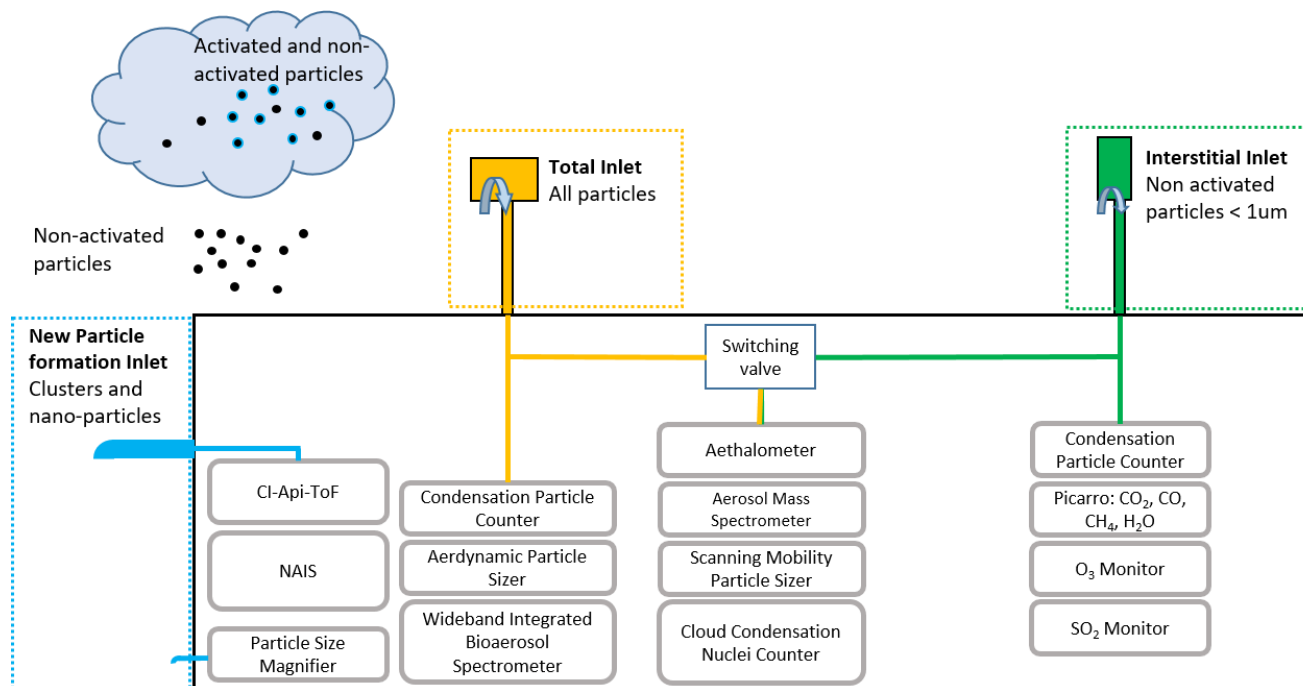
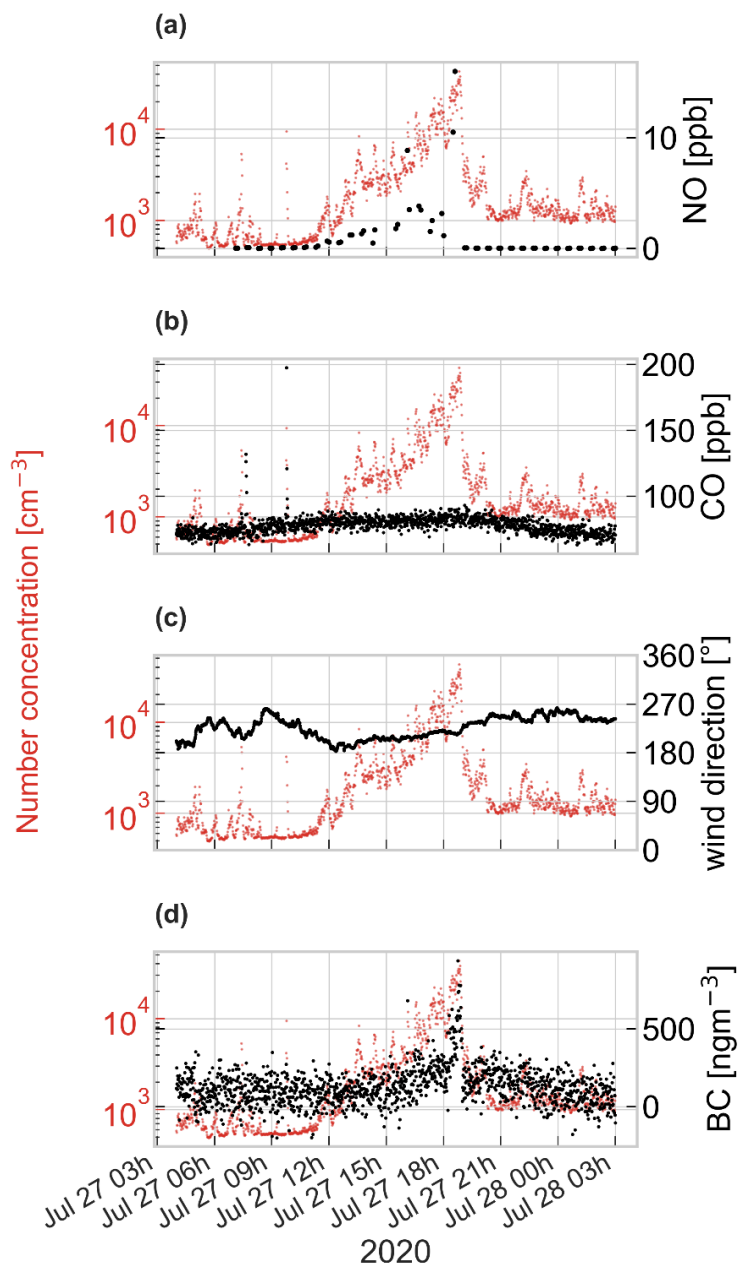


Figure A3: Full setup of the *Swiss Container* during the MOSAiC expedition (not all elements are discussed in this manuscript). In yellow the total inlet, in green the interstitial inlet. The valve switched between the two inlets to allow the instruments behind it (aethalometer, aerosol mass spectrometer, scanning mobility particle sizer, cloud condensation nuclei counter) to measure from both inlets. The blue inlet is the new particle formation inlet. CI-Api-ToF stands for chemical ionization atmospheric pressure interface time of flight mass spectrometer. NAIS stands for neutral cluster and air ion spectrometer.

660



665

Figure A4: Particle number concentration (left axis) along with a) NO (in parts per billion (ppb)), b) CO (in parts per billion (ppb)), c) relative wind direction and d) equivalent BC ( $\text{ng}/\text{m}^3$ ) at 880nm with standard manufacturer settings for the correction factor and mass absorption cross section during a local pollution event in the afternoon of July 27, 2020. Starting around noon, the particle number concentration, NO and BC concentrations increased as wind came from the stack. Note that CO concentrations did not exhibit any significant variability during that event.

670



**Figure A5:** A situation when the wind was coming from the stack's direction and the exhaust plume went directly over the *Swiss Container*, but due to the surface inversion no pollution spikes were measured in the *Swiss Container*. The container was located at the bow of the ship, below the crane (left hand side in this picture). Photo credit: Ivo Beck.

675

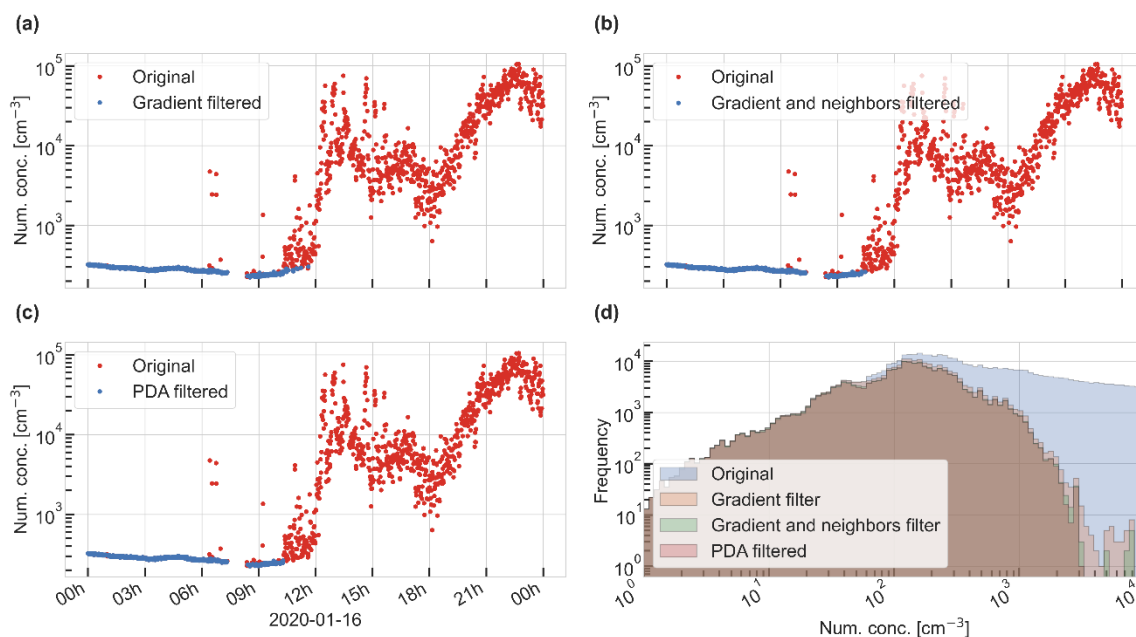
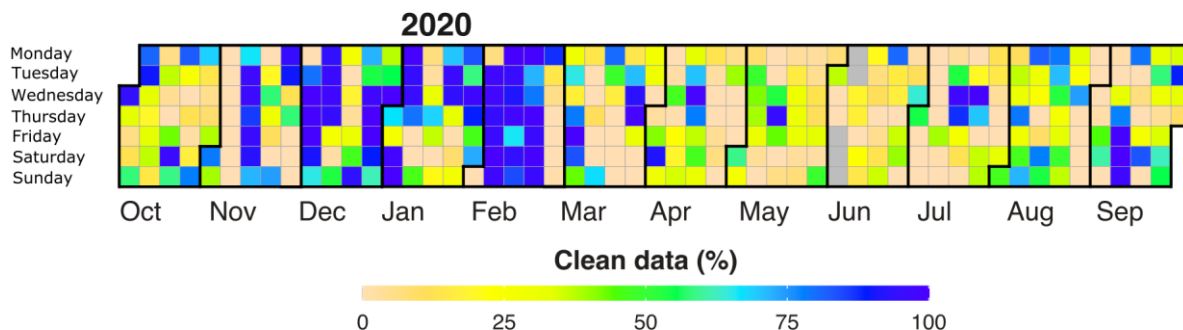
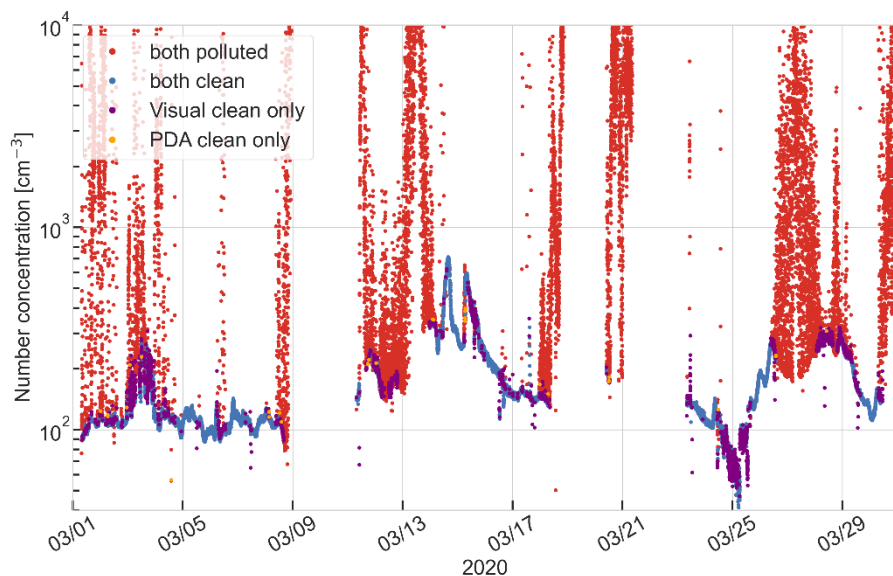


**Figure A6:** Same as Fig. 4 but for another day (January 16, 2020). Panels a-c show the original particle number concentrations data in red, overlaid with the unaffected data in blue. The application of additional filters in panels b and c do not show an effect. Panel d shows the distribution of the particle number concentrations of the complete dataset in blue, and after the application of different filters in orange, green and red.

680



685 **Figure A7: Percentage of clean particle number concentration data points per day during the MOSAiC expedition after application of the PDA. Missing data are indicated in grey and correspond to data removed when Polarstern was within Svalbard’s 12 nautical miles zone. Please note this figure is indicative only and does not necessarily reflect the percentage of clean data points collected by other instruments during the expedition.**



690 **Figure A8: Time series with a comparison of the visual identification method and the PDA in March, which was a month with many pollution events. In red: Data points which are detected as polluted by both methods. In blue: Data points which are detected as pollution-free by both methods. In purple: Data points which are detected as pollution-free only by the visual identification method. In orange: Data points which are detected as pollution-free only by the PDA.**



695

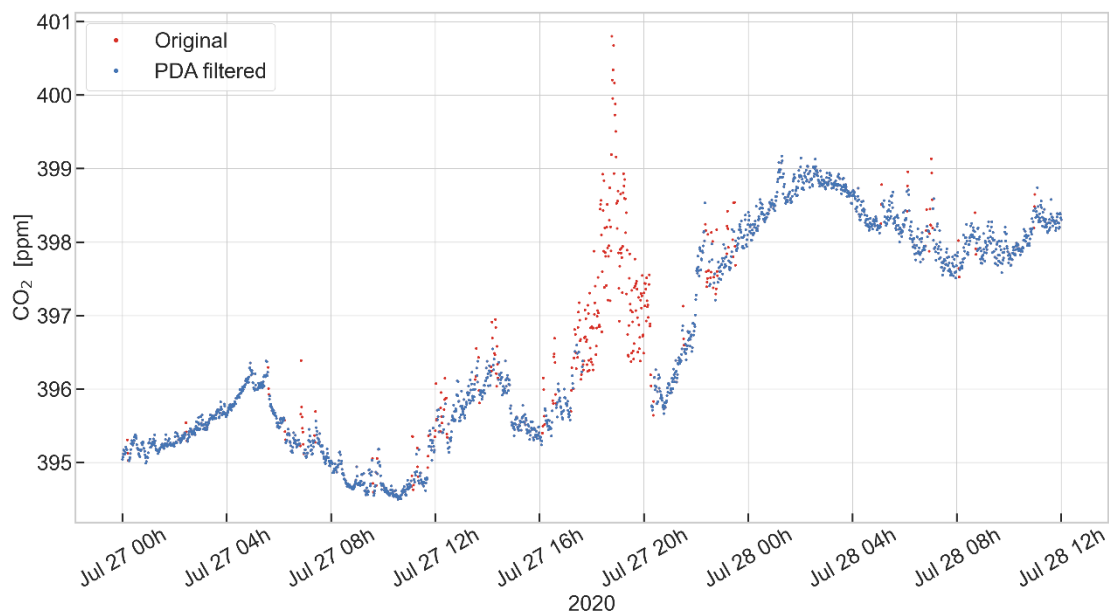
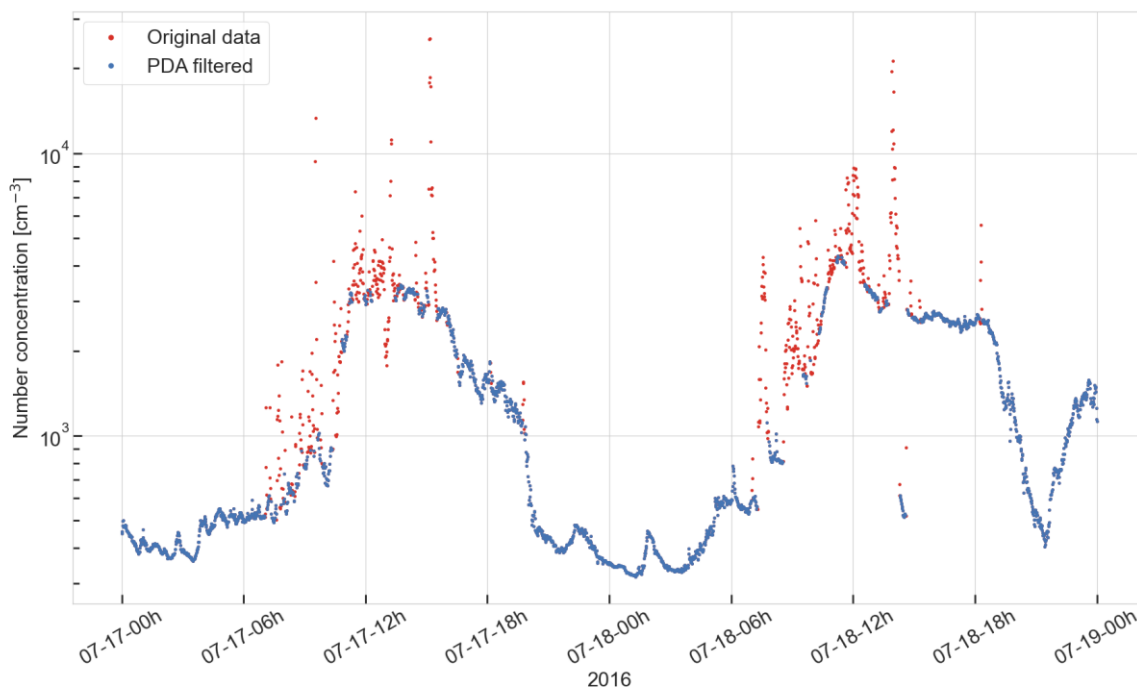
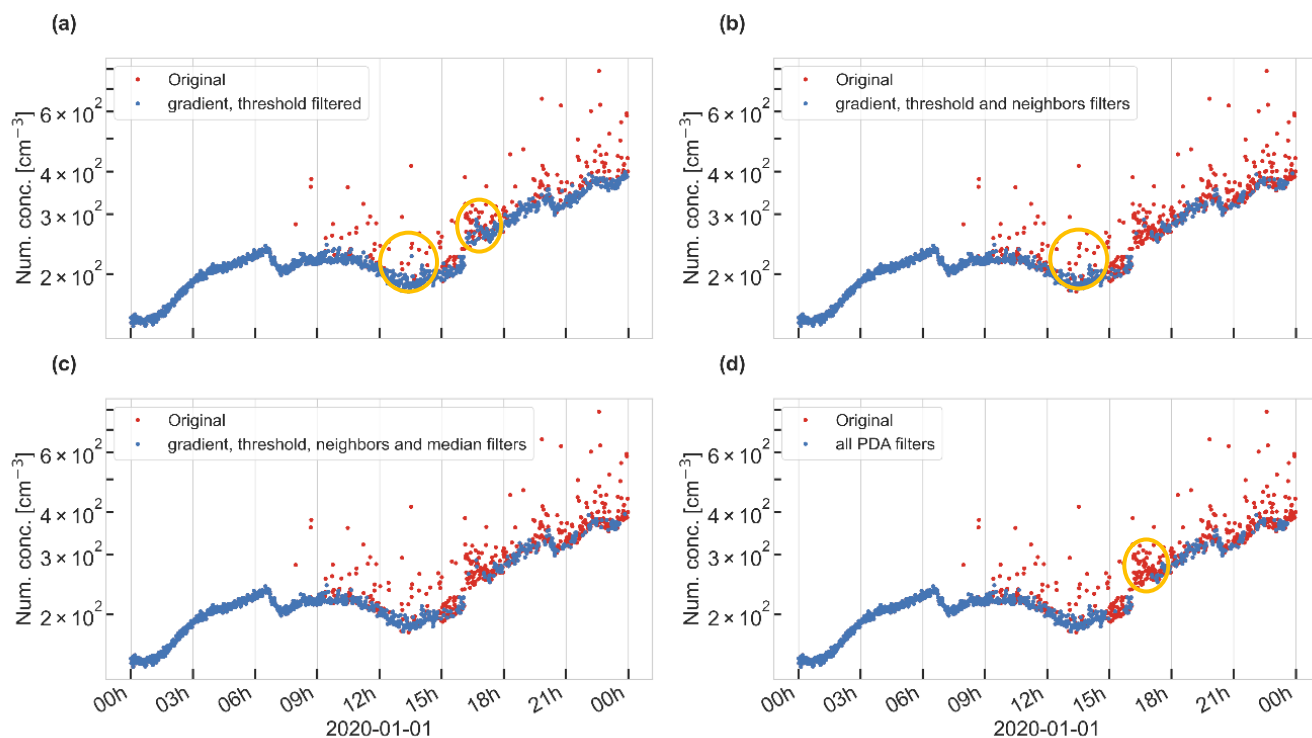


**Figure A9.** Time series of CO<sub>2</sub> mixing ratios after the application of the PDA using step 1B. Original data are shown in red, overlaid with unaffected data filtered by the PDA.



700 **Figure A10.** Time series of particle number concentration dataset from JFJ after the application of the PDA. Original data is shown in red, overlaid with unaffected data filtered by the PDA.



705

**Figure A11:** Case study of January 1, 2020. The particle number concentration signal is influenced by pollution which shows as a noisy signal and not in distinct spikes. Panels a-d show the original particle number concentrations data in red, overlaid with the unaffected data in blue after applying different filtering steps of the PDA. The orange circles highlight situations where applications of the neighbors filter and the sparse data filter improve the detection of polluted data significantly.

710

## Appendix B: Application of the PDA to various time-resolutions

We use the averaged time series from the gradient filter for further filtering steps in the PDA. This comes with the trade-off that the dataset loses time resolution when applying the PDA. In many applications this might not be a problem since data are often collected in higher time resolutions than needed for further analysis. We applied the PDA to the original dataset of the CPC 3025 (10 s time resolution). Figure B1a shows the gradients plotted against the total number concentrations for this dataset, which is used to determine the separation line (in red) for the gradient filter. It is less intuitive to find a good position of the separation line, compared to the one-minute averaged gradient (Fig. 3) because the two branches do not separate as clearly. We chose a separation line with the parameters  $a = 0.6 \text{ cm}^{-3}\text{s}^{-1}$  and  $m = 0.44 \text{ s}^{-1}$ . Figure B1b shows the same graph for the 10 min averaged time series of the same dataset. Here, we used  $a = 1 \text{ cm}^{-3}\text{s}^{-1}$  and  $m = 0.49 \text{ s}^{-1}$  for the separation line. In both cases, it is possible to distinguish between the two gradient branches, which indicates polluted and unaffected data. We observe that the separation line tends to go to higher gradients with coarser time resolution, which is a result of the longer

720



725 averaging time, because this smoothens the variability. Figure B2 shows the original (in red) and filtered (in blue) time series over three days after application of all PDA filtering steps to the two datasets (10 sec time resolution in panel a, and 10 min time resolution in panel b). The used parameters of the PDA are listed in table B1. The PDA detects the polluted spikes in both cases and is able to separate clean from polluted data. Even though the lower time resolution data do not have as distinct pollution "spikes". Potential outliers could have been smoothed when averaging. We conclude, the possibility to "tune" different parameters of the PDA makes it applicable to datasets with different temporal resolutions.

730 **Table B1: Parameters used for the application of the PDA to two datasets with different time resolutions**

Filter step	Parameter	Particle number concentration in 10 sec time resolution	Particle number concentration in 10 min time resolution
<b>1A. Gradient filter (Power law)</b>	a	$0.6 \text{ cm}^{-3}\text{s}^{-1}$	$1 \text{ cm}^{-3}\text{s}^{-1}$
	m	$0.44 \text{ s}^{-1}$	$0.49 \text{ s}^{-1}$
<b>2. Threshold filter</b>	Upper threshold	$10^4 \text{ cm}^{-3}$	$10^4 \text{ cm}^{-3}$
	Lower threshold	$60 \text{ cm}^{-3}$	$60 \text{ cm}^{-3}$
<b>3. Neighboring points filter</b>	On/off	On	On
<b>4. Median filter</b>	Median time window	30 min	60 min
	Median deviation factor	1.4	1.4
<b>5. Sparse data filter (no. of data points)</b>	Sparse window	180	12
	Sparse threshold	144	10

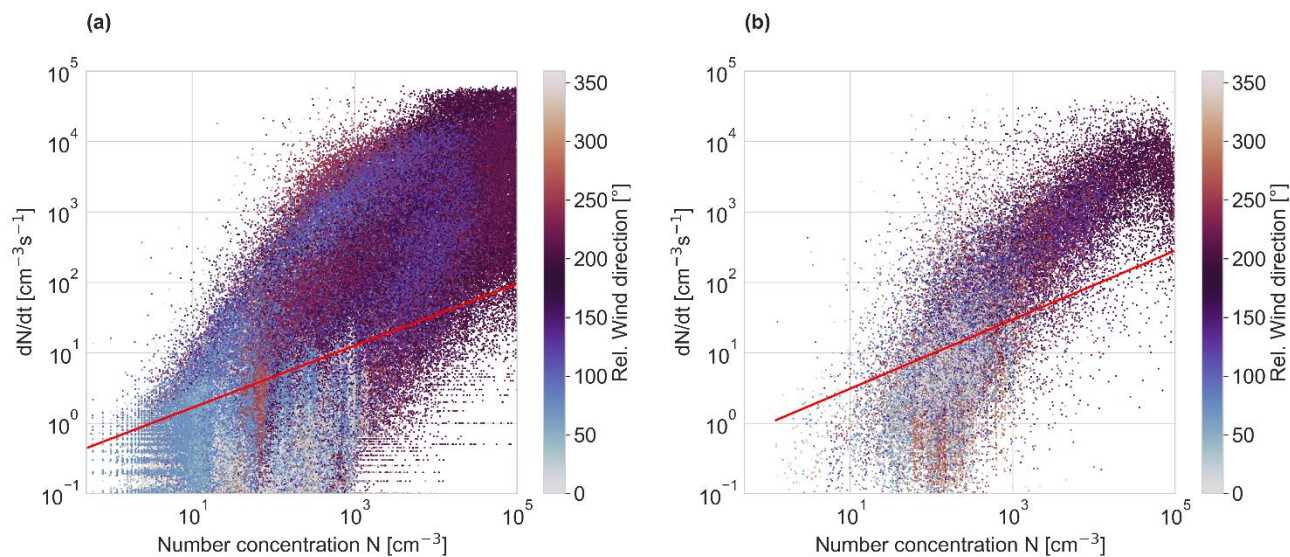


**Figure B1.** Relation of the absolute value of the particle number concentration gradient to the absolute number concentration for two different time resolutions. a: 10 sec, b: 10 min. The color-code indicates the relative wind direction. The red lines separate polluted from unaffected data points with a slope of  $0.44 \text{ s}^{-1}$  and an intercept of  $0.6 \text{ cm}^{-3}\text{s}^{-1}$  in panel a and a slope of  $0.49 \text{ s}^{-1}$  and an intercept of  $1 \text{ cm}^{-3}\text{s}^{-1}$  in panel b.

735

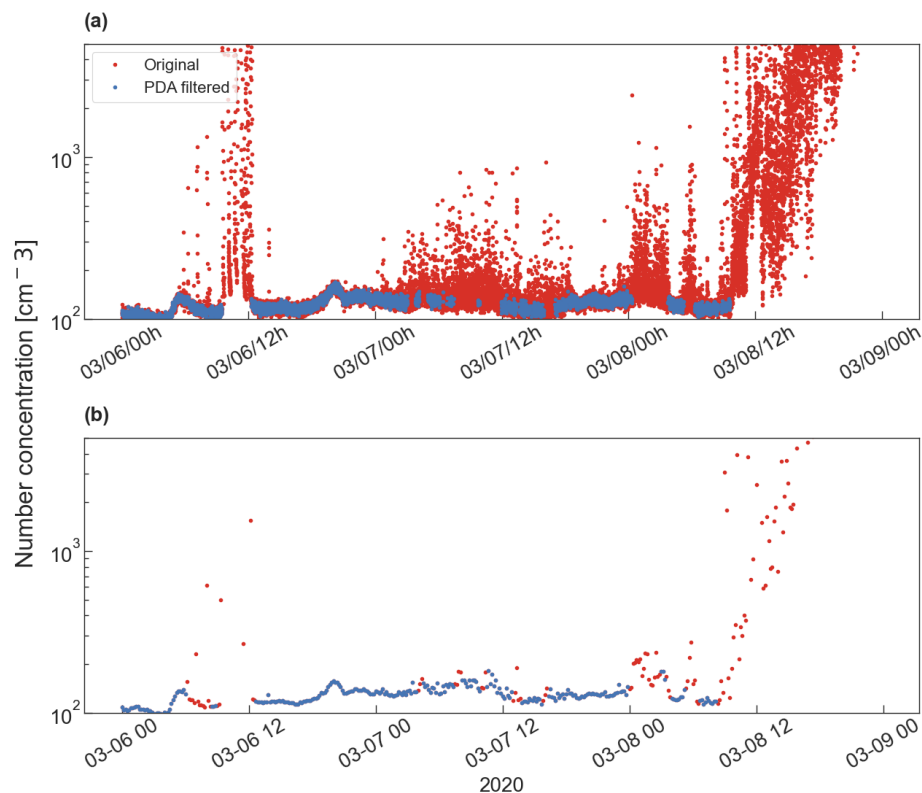


**Figure B2:** Performance test of the PDA on datasets with two different time resolutions. a) 10 sec time resolution data b) 10 min time resolution data. Filtered data in blue is shown on top of the original data of the corresponding time series in red.

#### 740 Code availability

The pollution mask code is available via zenodo (<https://doi.org/10.5281/zenodo.5761101>).

#### Data availability

All *Swiss Container* MOSAiC data will be publicly accessible from 1 January 2023 via PANGAEA. Datasets of the raw and the corrected particle number concentrations in 10s time resolution of the CPC 3025 were submitted to PANGAEA on  
745 December 6, 2021. A one minute averaged dataset of the CPC 3025, together with a pollution flag created by the PDA was submitted to PANGAEA on December 6, 2021. The ARM datasets are available via the ARM Data Discovery tool: <https://adc.arm.gov/discovery/#/> (Kuang et al., 2021). The Jungfraujoch data are available via [ebas.nilu.no](http://ebas.nilu.no).



### Author contributions

750 A.B. and I.B. developed the PDA. J.S. and H.A. conceived the manuscript idea. X.G. performed the visual data cleaning. L.D. provided AMS dataset, H.A. provided the trace gases datasets. N.B. and M.G.-B. provided the JFJ data. L.Q., I.B., J.S., T.J., T.L., H.A., M.B. performed measurements on board. I.B., H.A., J.S. wrote the manuscript. All authors commented on the manuscript.

### Competing of Interest

755 The authors declare no conflict of interest.

### Acknowledgements

Data used in this manuscript was produced as part of the international Multidisciplinary drifting Observatory for the Study of the Arctic Climate (MOSAiC) with the tag MOSAiC20192020 and the Project\_ID: AWI\_PS122\_00. We thank the land-based MOSAiC teams of the University of Helsinki and the Paul Scherrer Institute for their incessant support. We thank Byron Blomquist, Steve Archer, Jacques Hueber, Dean Howard, Hans-Werner Jacobi, Detlev Helmig, Ludovic Bariteau, and Kevin Posman for collecting and sharing the NO dataset used in the Appendix. We also thank Chongai Kuang from Brookhaven National Laboratory for providing support with the data used for the visual filtering method. The authors would like to thank the Polarstern crew and in particular the workshops for their fantastic support. We thank all those who contributed to MOSAiC and made this endeavour possible (Nixdorf et al., 2021). The Foundation High Altitude Research Stations Jungfrauoch & Gornergrat is acknowledged for supporting the measurements taken at Jungfrauoch. Datasets of the CPCf was obtained from the Atmospheric Radiation Measurement (ARM) User Facility, a U.S. Department of Energy (DOE) Office of Science User Facility managed by the Biological and Environmental Research Program. I.B. and H.A. received funding from the Swiss National Science Foundation (grant no. 200021\_188478). T.P. acknowledges funding through University of Helsinki (HY-ACTRIS) and Academy of Finland (333397) and Atmosphere and Climate Competence Center (ACCC, 337549). T.J. received funding from the Academy of Finland (334514) and acknowledges EMME-CARE, funded by the European Union's Horizon 2020 research and innovation programme under grant agreement No. 856612 and the Cyprus Government. LQ thanks the European Research Council ERC (GASPARCON – grant no 714621). Participation of the Swiss Container was co-financed by the Swiss Polar Institute and University of Helsinki. J.S. holds the Ingvar Kamrad Chair for Extreme Environments Research sponsored by Ferring Pharmaceuticals. Aerosol measurements at the Jungfrauoch are performed within the framework of the Swiss contribution to the Global Atmosphere Watch (GAW) program funded by MeteoSwiss. Further financial support was received through the ACTRIS2 project (EU H2020 grant no. 654109 and SERI contract no. 15.0159-1)

### References

780 Alfred-Wegener-Institut Helmholtz-Zentrum für Polar- und Meeresforschung: Polar Research and Supply Vessel POLARSTERN Operated by the Alfred-Wegener-Institute, Journal of large-scale research facilities, 3, 119, <https://doi.org/10.17815/jlsrf-3-163>, 2017.



- 785 Alroe, J., Cravigan, L. T., Miljevic, B., Johnson, G. R., Selleck, P., Humphries, R. S., Keywood, M. D., Chambers, S. D., Williams, A. G., and Ristovski, Z. D.: Marine productivity and synoptic meteorology drive summer-time variability in Southern Ocean aerosols, *Atmos. Chem. Phys.*, 20, 8047–8062, <https://doi.org/10.5194/acp-20-8047-2020>, 2020.
- 790 Angot, H., Blomquist, B., Howard, D., Archer, S. D., Bariteau, L., Beck, I., Boyer, M., Brasseur, Z., Helmig, D., Hueber, J., Jacobi, H.-W., Jokinen, T., Laurila, T., Posman, K., Quéléver, L. L. J., Shupe, M. D., and Schmale, J.: Year-round trace gas measurements in the Central Arctic during the MOSAiC expedition, submission to *Scientific Data*, MOSAiC special issue, in prep.
- 795 Asmi, A., Collaud Coen, M., Ogren, J. A., Andrews, E., Sheridan, P., Jefferson, A., Weingartner, E., Baltensperger, U., Bukowiecki, N., Lihavainen, H., Kivekäs, N., Asmi, E., Aalto, P. P., Kulmala, M., Wiedensohler, A., Birmili, W., Hamed, A., O’Dowd, C., G Jennings, S., Weller, R., Flentje, H., Fjaeraa, A. M., Fiebig, M., Myhre, C. L., Hallar, A. G., Swietlicki, E., Kristensson, A., and Laj, P.: Aerosol decadal trends – Part 2: In-situ aerosol particle number concentrations at GAW and ACTRIS stations, *Atmos. Chem. Phys.*, 13, 895–916, <https://doi.org/10.5194/acp-13-895-2013>, 2013.
- 800 Asmi, E., Kondratyev, V., Brus, D., Laurila, T., Lihavainen, H., Backman, J., Vakkari, V., Aurela, M., Hatakka, J., Viisanen, Y., Uttal, T., Ivakhov, V., and Makshtas, A.: Aerosol size distribution seasonal characteristics measured in Tiksi, Russian Arctic, *Atmos. Chem. Phys.*, 16, 1271–1287, <https://doi.org/10.5194/acp-16-1271-2016>, 2016.
- Baccarini, A.: Investigation of New Aerosol Particle Formation in Polar Regions, Doctoral Thesis, ETH Zurich, <https://doi.org/10.3929/ethz-b-000502951>, 2021.
- 805 Baccarini, A., Karlsson, L., Dommen, J., Duplessis, P., Vüllers, J., Brooks, I. M., Saiz-Lopez, A., Salter, M., Tjernström, M., Baltensperger, U., Zieger, P., and Schmale, J.: Frequent new particle formation over the high Arctic pack ice by enhanced iodine emissions, *Nat. Commun.*, 11, 4924, <https://doi.org/10.1038/s41467-020-18551-0>, 2020.
- 810 Beck, L. J., Sarnela, N., Junninen, H., Hoppe, C. J. M., Garmash, O., Bianchi, F., Riva, M., Rose, C., Peräkylä, O., Wimmer, D., Kausiala, O., Jokinen, T., Ahonen, L., Mikkilä, J., Hakala, J., He, X.-C., Kontkanen, J., Wolf, K. K. E., Cappelletti, D., Mazzola, M., Traversi, R., Petroselli, C., Viola, A. P., Vitale, V., Lange, R., Massling, A., Nøjgaard, J. K., Krejci, R., Karlsson, L., Zieger, P., Jang, S., Lee, K., Vakkari, V., Lampilahti, J., Thakur, R. C., Leino, K., Kangasluoma, J., Duplissy, E.-M., Siivola, E., Marbouti, M., Tham, Y. J., Saiz-Lopez, A., Petäjä, T., Ehn, M., Worsnop, D. R., Skov, H., Kulmala, M., Kerminen, V.-M., and Sipilä, M.: Differing Mechanisms of New Particle Formation at Two Arctic Sites, *Geophys. Res. Lett.*, 48, e2020GL091334, <https://doi.org/10.1029/2020GL091334>, 2021.
- 815 Bukowiecki, N., Dommen, J., Prévôt, A. S. H., Richter, R., Weingartner, E., and Baltensperger, U.: A mobile pollutant measurement laboratory—measuring gas phase and aerosol ambient concentrations with high spatial and temporal resolution, *Atmos. Environ.*, 36, 5569–5579, [https://doi.org/10.1016/S1352-2310\(02\)00694-5](https://doi.org/10.1016/S1352-2310(02)00694-5), 2002.



- 820 Bukowiecki, N., Weingartner, E., Gysel, M., Collaud Coen, M., Zieger, P., Herrmann, E., Steinbacher, M., Gäggeler, H. W., and Baltensperger, U.: A review of more than 20 years of aerosol observation at the high altitude research station Jungfraujoch, Switzerland (3580 m asl), *Aerosol Air Qual. Res.*, 16, 764–788, <https://doi.org/10.4209/aaqr.2015.05.0305>, 2016.
- 825 Bukowiecki, N., Brem, B. T., Wehrle, G., Močnik, G., Affolter, S., Leuenberger, M., Coen, M. C., Hervo, M., Baltensperger, U., and Gysel-Beer, M.: Elucidating local pollution and site representativeness at the Jungfraujoch, Switzerland through parallel aerosol measurements at an adjacent mountain ridge, *Environmental Research Communications*, 3, 021001, <https://doi.org/10.1088/2515-7620/abe987>, 2021.
- Carslaw, K. S., Boucher, O., Spracklen, D. V., Mann, G. W., Rae, J. G. L., Woodward, S., and Kulmala, M.: A review of natural aerosol interactions and feedbacks within the Earth system, *Atmos. Chem. Phys.*, 10, 1701–1737, <https://doi.org/10.5194/acp-10-1701-2010>, 2010.
- 830 Cox, M. L., Sturrock, G. A., Fraser, P. J., Siems, S. T., Krummel, P. B., and O’Doherty, S.: Regional Sources of Methyl Chloride, Chloroform and Dichloromethane Identified from AGAGE Observations at Cape Grim, Tasmania, 1998–2000, *J. Atmos. Chem.*, 45, 79–99, <https://doi.org/10.1023/A:1024022320985>, 2003.
- 835 Dada, L., Beck, I., Quéléver, L. L. J., Baccharini, A., Angot, H., Laurila, T., Brasseur, Z., Boyer, M., Jozef, G., De Boer, G., Henning, S., Daellenbach, K. R., Jokinen, T., and Schmale, J.: A central Arctic extreme aerosol even triggered by a warm air mass intrusion, in prep.
- 840 DeCarlo, P. F., Kimmel, J. R., Trimborn, A., Northway, M. J., Jayne, J. T., Aiken, A. C., Gonin, M., Fuhrer, K., Horvath, T., Docherty, K. S., Worsnop, D. R., and Jimenez, J. L.: Field-Deployable, High-Resolution, Time-of-Flight Aerosol Mass Spectrometer, *Anal. Chem.*, 78, 8281–8289, <https://doi.org/10.1021/ac061249n>, 2006.
- Drewnick, F., Böttger, T., von der Weiden-Reinmüller, S.-L., Zorn, S. R., Klimach, T., Schneider, J., and Borrmann, S.: Design of a mobile aerosol research laboratory and data processing tools for effective stationary and mobile field measurements, *Atmos. Meas. Tech.*, 5, 1443–1457, <https://doi.org/10.5194/amt-5-1443-2012>, 2012.
- 845 El Yazidi, A., Ramonet, M., Ciais, P., Broquet, G., Pison, I., Abbaris, A., Brunner, D., Conil, S., Delmotte, M., Gheusi, F., Guerin, F., Hazan, L., Kachroudi, N., Kouvarakis, G., Mihalopoulos, N., Rivier, L., and Serça, D.: Identification of spikes associated with local sources in continuous time series of atmospheric CO, CO<sub>2</sub> and CH<sub>4</sub>, *Atmos. Meas. Tech.*, 11, 1599–1614, <https://doi.org/10.5194/amt-11-1599-2018>, 2018.
- 850 Enroth, J., Saarikoski, S., Niemi, J., Kousa, A., Ježek, I., Močnik, G., Carbone, S., Kuuluvainen, H., Rönkkö, T., Hillamo, R., and Pirjola, L.: Chemical and physical characterization of traffic particles in four different highway environments in the Helsinki metropolitan area, *Atmos. Chem. Phys.*, 16, 5497–5512, <https://doi.org/10.5194/acp-16-5497-2016>, 2016.



- Enroth, J., Kangasluoma, J., Korhonen, F., Hering, S., Picard, D., Lewis, G., Attoui, M., and Petäjä, T.:  
855 On the time response determination of condensation particle counters, *Aerosol Sci. Tech.*, 52, 778–787,  
<https://doi.org/10.1080/02786826.2018.1460458>, 2018.
- Fontijn, A., Sabadell, A. J., and Ronco, R. J.: Homogeneous chemiluminescent measurement of nitric  
oxide with ozone. Implications for continuous selective monitoring of gaseous air pollutants, *Anal.*  
*Chem.*, 42, 575–579, <https://doi.org/10.1021/ac60288a034>, 1970.
- 860 Freud, E., Krejci, R., Tunved, P., Leitch, R., Nguyen, Q. T., Massling, A., Skov, H., and Barrie, L.: Pan-  
Arctic aerosol number size distributions: seasonality and transport patterns, *Atmos. Chem. Phys.*, 17,  
8101–8128, <https://doi.org/10.5194/acp-17-8101-2017>, 2017.
- Frossard, A. A., Russell, L. M., Burrows, S. M., Elliott, S. M., Bates, T. S., and Quinn, P. K.: Sources  
and composition of submicron organic mass in marine aerosol particles: Marine Aerosol Organic Mass  
865 Composition, *J. Geophys. Res. Atmos.*, 119, 12,977–13,003, <https://doi.org/10.1002/2014JD021913>,  
2014.
- Herrmann, E., Weingartner, E., Henne, S., Vuilleumier, L., Bukowiecki, N., Steinbacher, M., Conen, F.,  
Collaud Coen, M., Hammer, E., Jurányi, Z., Baltensperger, U., and Gysel, M.: Analysis of long-term  
870 aerosol size distribution data from Jungfraujoch with emphasis on free tropospheric conditions, cloud  
influence, and air mass transport, *J. Geophys. Res. Atmos.*, 120, 9459–9480,  
<https://doi.org/10.1002/2015JD023660>, 2015.
- Humphries, R. S., Klekociuk, A. R., Schofield, R., Keywood, M., Ward, J., and Wilson, S. R.:  
Unexpectedly high ultrafine aerosol concentrations above East Antarctic sea ice, *Atmos. Chem. Phys.*,  
16, 2185–2206, <https://doi.org/10.5194/acp-16-2185-2016>, 2016.
- 875 Humphries, R. S., McRobert, I. M., Ponsonby, W. A., Ward, J. P., Keywood, M. D., Loh, Z. M., Krummel,  
P. B., and Harnwell, J.: Identification of platform exhaust on the RV Investigator, *Atmos. Meas. Tech.*,  
12, 3019–3038, <https://doi.org/10.5194/amt-12-3019-2019>, 2019.
- Kolesar, K. R., Cellini, J., Peterson, P. K., Jefferson, A., Tuch, T., Birmili, W., Wiedensohler, A., and  
Pratt, K. A.: Effect of Prudhoe Bay emissions on atmospheric aerosol growth events observed in  
880 Utqiagvik (Barrow), Alaska, *Atmos. Environ.*, 152, 146–155,  
<https://doi.org/10.1016/j.atmosenv.2016.12.019>, 2017.
- Kuang, C., Salwen, C., Boyer, M., and Singh, A.: Condensation Particle Counter (AOSCPCF),  
Atmospheric Radiation Measurement (ARM) user facility, 2021. <https://doi.org/10.5439/1046184>,  
Accessed December 6.
- 885 Kulmala, M., Petäjä, T., Ehn, M., Thornton, J., Sipilä, M., Worsnop, D. r., and Kerminen, V.-M.:  
Chemistry of Atmospheric Nucleation: On the Recent Advances on Precursor Characterization and



- Atmospheric Cluster Composition in Connection with Atmospheric New Particle Formation, *Annu. Rev. Phys. Chem.*, 65, 21–37, <https://doi.org/10.1146/annurev-physchem-040412-110014>, 2014.
- 890 Kyrö, E.-M., Kerminen, V.-M., Virkkula, A., Dal Maso, M., Parshintsev, J., Ruíz-Jimenez, J., Forsström, L., Manninen, H. E., Riekkola, M.-L., Heinonen, P., and Kulmala, M.: Antarctic new particle formation from continental biogenic precursors, *Atmos. Chem. Phys.*, 13, 3527–3546, <https://doi.org/10.5194/acp-13-3527-2013>, 2013.
- 895 Leck, C., Bigg, E. K., Covert, D. S., Heintzenberg, J., Maenhaut, W., Nilsson, E. D., and Wiedensohler, A.: Overview of the atmospheric research program during the International Arctic Ocean Expedition of 1991 (IAOE-91) and its scientific results, *Tellus B: Chemical and Physical Meteorology*, 48, 136–155, <https://doi.org/10.3402/tellusb.v48i2.15833>, 1996.
- 900 Maslanik, J. and Stroeve, J.: Near-Real-Time DMSP SSMIS Daily Polar Gridded Sea Ice Concentrations, Version 1, September 2019, Boulder, Colorado USA. NASA National Snow and Ice Data Center Distributed Active Archive Center., <https://doi.org/10.5067/U8C09DWVX9LM>, 1999. Accessed in August 2021.
- 905 Massoli, P., Fortner, E. C., Canagaratna, M. R., Williams, L. R., Zhang, Q., Sun, Y., Schwab, J. J., Trimborn, A., Onasch, T. B., Demerjian, K. L., Kolb, C. E., Worsnop, D. R., and Jayne, J. T.: Pollution Gradients and Chemical Characterization of Particulate Matter from Vehicular Traffic near Major Roadways: Results from the 2009 Queens College Air Quality Study in NYC, *Aerosol Sci. Tech.*, 46, 1201–1218, <https://doi.org/10.1080/02786826.2012.701784>, 2012.
- 910 McFarquhar, G. M., Bretherton, C. S., Marchand, R., Protat, A., DeMott, P. J., Alexander, S. P., Roberts, G. C., Twohy, C. H., Toohey, D., Siems, S., Huang, Y., Wood, R., Rauber, R. M., Lasher-Trapp, S., Jensen, J., Stith, J. L., Mace, J., Um, J., Järvinen, E., Schnaiter, M., Gettelman, A., Sanchez, K. J., McCluskey, C. S., Russell, L. M., McCoy, I. L., Atlas, R. L., Bardeen, C. G., Moore, K. A., Hill, T. C. J., Humphries, R. S., Keywood, M. D., Ristovski, Z., Cravigan, L., Schofield, R., Fairall, C., Mallet, M. D., Kreidenweis, S. M., Rainwater, B., D’Alessandro, J., Wang, Y., Wu, W., Saliba, G., Levin, E. J. T., Ding, S., Lang, F., Truong, S. C. H., Wolff, C., Haggerty, J., Harvey, M. J., Klekociuk, A. R., and McDonald, A.: Observations of Clouds, Aerosols, Precipitation, and Surface Radiation over the Southern Ocean: An Overview of CAPRICORN, MARCUS, MICRE, and SOCRATES, *B. Am. Meteorol. Soc.*, 102, E894–E928, <https://doi.org/10.1175/BAMS-D-20-0132.1>, 2021.
- 915 Moallemi, A., Landwehr, S., Robinson, C., Simó, R., Zamanillo, M., Chen, G., Baccarini, A., Schnaiter, M., Henning, S., Modini, R. L., Gysel-Ber, M., and Schmale, J.: Sources, Occurrence and Characteristics of Fluorescent Biological Aerosol Particles Measured Over the Pristine Southern Ocean, *J. Geophys. Res. Atmos.*, 126, e2021JD034811, <https://doi.org/10.1029/2021JD034811>, 2021.
- 920 Nixdorf, U., Dethloff, K., Rex, M., Shupe, M., Sommerfeld, A., Perovich, D. K., Nicolaus, M., Heuzé, C., Rabe, B., Loose, B., Damm, E., Gradinger, R., Fong, A., Maslowski, W., Rinke, A., Kwok, R., Spreen, G., Wendisch, M., Herber, A., Hirsekorn, M., Mohaupt, V., Frickenhaus, S., Immerz, A., Weiss-Tuider,



- 925 K., König, B., Menedoht, D., Regnery, J., Gerchow, P., Ransby, D., Krumpfen, T., Morgenstern, A., Haas, C., Kanzow, T., Rack, F. R., Saitzev, V., Sokolov, V., Makarov, A., Schwarze, S., Wunderlich, T., Wurr, K., and Boetius, A.: MOSAiC Extended Acknowledgement, <https://doi.org/10.5281/zenodo.5541624>, 2021.
- 930 Reddington, C. L., Carslaw, K. S., Stier, P., Schutgens, N., Coe, H., Liu, D., Allan, J., Browse, J., Pringle, K. J., Lee, L. A., Yoshioka, M., Johnson, J. S., Regayre, L. A., Spracklen, D. V., Mann, G. W., Clarke, A., Hermann, M., Henning, S., Wex, H., Kristensen, T. B., Leaitch, W. R., Pöschl, U., Rose, D., Andreae, M. O., Schmale, J., Kondo, Y., Oshima, N., Schwarz, J. P., Nenes, A., Anderson, B., Roberts, G. C., Snider, J. R., Leck, C., Quinn, P. K., Chi, X., Ding, A., Jimenez, J. L., and Zhang, Q.: The Global Aerosol Synthesis and Science Project (GASSP): Measurements and Modeling to Reduce Uncertainty, *B. Am. Meteorol. Soc.*, 98, 1857–1877, <https://doi.org/10.1175/BAMS-D-15-00317.1>, 2017.
- 935 Ruckstuhl, A. F., Henne, S., Reimann, S., Steinbacher, M., Vollmer, M. K., O’Doherty, S., Buchmann, B., and Hueglin, C.: Robust extraction of baseline signal of atmospheric trace species using local regression, *Atmos. Meas. Tech.*, 5, 2613–2624, <https://doi.org/10.5194/amt-5-2613-2012>, 2012.
- Schmale, J. and Baccharini, A.: Progress in Unraveling Atmospheric New Particle Formation and Growth Across the Arctic, *Geophys. Res. Lett.*, 48, e2021GL094198, <https://doi.org/10.1029/2021GL094198>, 2021.
- 940 Schmale, J., Schneider, J., Nemitz, E., Tang, Y. S., Dragosits, U., Blackall, T. D., Trathan, P. N., Phillips, G. J., Sutton, M., and Braban, C. F.: Sub-Antarctic marine aerosol: dominant contributions from biogenic sources, *Atmos. Chem. Phys.*, 13, 8669–8694, <https://doi.org/10.5194/acp-13-8669-2013>, 2013.
- 945 Schmale, J., Henning, S., Henzing, B., Keskinen, H., Sellegri, K., Ovadnevaite, J., Bougiatioti, A., Kalivitis, N., Stavroulas, I., Jefferson, A., Park, M., Schlag, P., Kristensson, A., Iwamoto, Y., Pringle, K., Reddington, C., Aalto, P., Äijälä, M., Baltensperger, U., Bialek, J., Birmili, W., Bukowiecki, N., Ehn, M., Fjærraa, A. M., Fiebig, M., Frank, G., Fröhlich, R., Frumau, A., Furuya, M., Hammer, E., Heikkinen, L., Herrmann, E., Holzinger, R., Hyono, H., Kanakidou, M., Kiendler-Scharr, A., Kinouchi, K., Kos, G., Kulmala, M., Mihalopoulos, N., Motos, G., Nenes, A., O’Dowd, C., Paramonov, M., Petäjä, T., Picard, D., Poulain, L., Prévôt, A. S. H., Slowik, J., Sonntag, A., Swietlicki, E., Svenningsson, B., Tsurumaru, H., Wiedensohler, A., Wittbom, C., Ogren, J. A., Matsuki, A., Yum, S. S., Myhre, C. L., Carslaw, K., Stratmann, F., and Gysel, M.: Collocated observations of cloud condensation nuclei, particle size distributions, and chemical composition, *Sci. Data*, 4, 170003, <https://doi.org/10.1038/sdata.2017.3>, 2017.
- 950 Schmale, J., Henning, S., Decesari, S., Henzing, B., Keskinen, H., Sellegri, K., Ovadnevaite, J., Pöhlker, M. L., Brito, J., Bougiatioti, A., Kristensson, A., Kalivitis, N., Stavroulas, I., Carbone, S., Jefferson, A., Park, M., Schlag, P., Iwamoto, Y., Aalto, P., Äijälä, M., Bukowiecki, N., Ehn, M., Frank, G., Fröhlich, R., Frumau, A., Herrmann, E., Herrmann, H., Holzinger, R., Kos, G., Kulmala, M., Mihalopoulos, N., Nenes, A., O’Dowd, C., Petäjä, T., Picard, D., Pöhlker, C., Pöschl, U., Poulain, L., Prévôt, A. S. H., Swietlicki, E., Andreae, M. O., Artaxo, P., Wiedensohler, A., Ogren, J., Matsuki, A., Yum, S. S.,



960 Stratmann, F., Baltensperger, U., and Gysel, M.: Long-term cloud condensation nuclei number concentration, particle number size distribution and chemical composition measurements at regionally representative observatories, *Atmos. Chem. Phys.*, 18, 2853–2881, <https://doi.org/10.5194/acp-18-2853-2018>, 2018.

965 Schmale, J., Baccarini, A., Thurnherr, I., Henning, S., Efraim, A., Regayre, L., Bolas, C., Hartmann, M., Welti, A., Lehtipalo, K., Aemisegger, F., Tatzelt, C., Landwehr, S., Modini, R. L., Tummon, F., Johnson, J. S., Harris, N., Schnaiter, M., Toffoli, A., Derkani, M., Bukowiecki, N., Stratmann, F., Dommen, J., Baltensperger, U., Wernli, H., Rosenfeld, D., Gysel-Beer, M., and Carslaw, K. S.: Overview of the Antarctic Circumnavigation Expedition: Study of Preindustrial-like Aerosols and Their Climate Effects (ACE-SPACE), *B. Am. Meteorol. Soc.*, 100, 2260–2283, <https://doi.org/10.1175/BAMS-D-18-0187.1>,  
970 2019.

Schmithuesen, H.: Continuous meteorological surface measurement during POLARSTERN cruise PS122/1, Alfred Wegener Institute, Helmholtz Centre for Polar and Marine Research, Bremerhaven, PANGAEA, <https://doi.org/10.1594/PANGAEA.935221>, 23 August 2021a.

975 Schmithuesen, H.: Continuous meteorological surface measurement during POLARSTERN cruise PS122/2, Alfred Wegener Institute, Helmholtz Centre for Polar and Marine Research, Bremerhaven, PANGAEA, <https://doi.org/10.1594/PANGAEA.935222>, 23 August 2021b.

Schmithuesen, H.: Continuous meteorological surface measurement during POLARSTERN cruise PS122/3, Alfred Wegener Institute, Helmholtz Centre for Polar and Marine Research, Bremerhaven, PANGAEA, <https://doi.org/10.1594/PANGAEA.935223>, 23 August 2021c.

980 Schmithuesen, H.: Continuous meteorological surface measurement during POLARSTERN cruise PS122/4, Alfred Wegener Institute, Helmholtz Centre for Polar and Marine Research, Bremerhaven, PANGAEA, <https://doi.org/10.1594/PANGAEA.935224>, 23 August 2021d.

985 Schmithuesen, H.: Continuous meteorological surface measurement during POLARSTERN cruise PS122/5, Alfred Wegener Institute, Helmholtz Centre for Polar and Marine Research, Bremerhaven, PANGAEA, <https://doi.org/10.1594/PANGAEA.935225>, 23 August 2021e.

Shupe, M. D., Rex, M., Blomquist, B., Persson, P. O. G., Schmale J., Uttal, T., Althausen, D., Angot, H., Archer, S., Bariteau, L., Beck, I., Bilberry, J., Bucci, S., Buck, C., Boyer, M., Brasseur, Z., Brooks, I. M., Calmer R., Cassano J., Castro V., Chu, D., Costa, D., Cox, C. J., Creamean, J., Crewell, S., Dahlke, S., Damm, E., de Boer, G., Deckelmann, H., Dethloff, K., Dütsch, M., Ebell, K., Ehrlich, A., Ellis, J.,  
990 Engelmann, R., Fong, A. A., Frey, M. M., Gallagher, M. R., Ganzeveld, L., Gradinger R., Graeser, J., Greenamyre, V., Griesche, H., Griffiths, S., Hamilton, J., Heinemann, G., Helmig, D., Herber A., Heuzé C., Hofer, J., Houchens, T., Howard, D., Inoue J., Jacobi, H. W., Jaiser, R., Jokinen, T., Jourdan, O., Jozef, G., King, W., Kirchgaessner, A., Klingebiel, M., Krassovski, M., Krumpfen, T., Lampert, A., Landing, W., Laurila, T., Lawrence, D., Lonardi, M., Loose, B., Lüpkes, C., Maahn, M., Macke, A.,  
995 Maslowski, W., Marsay, C., Maturilli, M., Mech, M., Morris, S., Moser, M., Nicolaus, M., Ortega, P.,



- 1000 Osborn, J., Pätzold F., Perovich, D. K., Petäjä, T., Pilz, C., Pirazzini, R., Posman, K., Powers, H., Pratt, K. A., Preußner, A., Quéléver, L., Radenz, M., Rabe, B., Rinke, A., Sachs, T., Schulz, A., Siebert, H., Silva, T., Solomon, A., Sommerfeld, A., Spreen, G., Stephens, M., Stohl, A., Svensson, G., Uin, J., Viegas, J., Voigt, C., von der Gathen, P., Wehner, B., Welker, J. M., Wendisch, M., Werner, M., Xie, Z., and Yue, F.: Overview of the MOSAiC Expedition – Atmosphere, *Elementa*, 86, under review.
- 1005 Tjernström, M., Leck, C., Birch, C. E., Bottenheim, J. W., Brooks, B. J., Brooks, I. M., Bäcklin, L., Chang, R. Y.-W., de Leeuw, G., Di Liberto, L., de la Rosa, S., Granath, E., Graus, M., Hansel, A., Heintzenberg, J., Held, A., Hind, A., Johnston, P., Knulst, J., Martin, M., Matrai, P. A., Mauritsen, T., Müller, M., Norris, S. J., Orellana, M. V., Orsini, D. A., Paatero, J., Persson, P. O. G., Gao, Q., Rauschenberg, C., Ristovski, Z., Sedlar, J., Shupe, M. D., Sierau, B., Sirevaag, A., Sjogren, S., Stetzer, O., Swietlicki, E., Szczodrak, M., Vaattovaara, P., Wahlberg, N., Westberg, M., and Wheeler, C. R.: The Arctic Summer Cloud Ocean Study (ASCOS): overview and experimental design, *Atmos. Chem. Phys.*, 14, 2823–2869, <https://doi.org/10.5194/acp-14-2823-2014>, 2014.
- 1010 Uin, J., Aiken, A. C., Dubey, M. K., Kuang, C., Pekour, M., Salwen, C., Sedlacek, A. J., Senum, G., Smith, S., Wang, J., Watson, T. B., and Springston, S. R.: Atmospheric Radiation Measurement (ARM) Aerosol Observing Systems (AOS) for Surface-Based In Situ Atmospheric Aerosol and Trace Gas Measurements, *J. Atmos. Ocean. Tech.*, 36, 2429–2447, <https://doi.org/10.1175/JTECH-D-19-0077.1>, 2019.
- 1015 Uttal, T., Curry, J. A., McPhee, M. G., Perovich, D. K., Moritz, R. E., Maslanik, J. A., Guest, P. S., Stern, H. L., Moore, J. A., Turenne, R., Heiberg, A., Serreze, M. C., Wylie, D. P., Persson, O. G., Paulson, C. A., Halle, C., Morison, J. H., Wheeler, P. A., Makshtas, A., Welch, H., Shupe, M. D., Intrieri, J. M., Stamnes, K., Lindsey, R. W., Pinkel, R., Pegau, W. S., Stanton, T. P., and Grenfeld, T. C.: Surface Heat Budget of the Arctic Ocean, *B. Am. Meteorol. Soc.*, 83, 255–275, [https://doi.org/10.1175/1520-0477\(2002\)083<0255:SHBOTA>2.3.CO;2](https://doi.org/10.1175/1520-0477(2002)083<0255:SHBOTA>2.3.CO;2), 2002.
- 1020 Uttal, T., Starkweather, S., Drummond, J. R., Vihma, T., Makshtas, A. P., Darby, L. S., Burkhardt, J. F., Cox, C. J., Schmeisser, L. N., Haiden, T., Maturilli, M., Shupe, M. D., Boer, G. D., Saha, A., Grachev, A. A., Crepinsek, S. M., Bruhwiler, L., Goodison, B., McArthur, B., Walden, V. P., Dlugokencky, E. J., Persson, P. O. G., Lesins, G., Laurila, T., Ogren, J. A., Stone, R., Long, C. N., Sharma, S., Massling, A., Turner, D. D., Stanitski, D. M., Asmi, E., Aurela, M., Skov, H., Eleftheriadis, K., Virkkula, A., Platt, A., Førlund, E. J., Iijima, Y., Nielsen, I. E., Bergin, M. H., Candlish, L., Zimov, N. S., Zimov, S. A., O'Neill, N. T., Fogal, P. F., Kivi, R., Konopleva-Akish, E. A., Verlinde, J., Kustov, V. Y., Vasel, B., Ivakhov, V. M., Viisanen, Y., and Intrieri, J. M.: International Arctic Systems for Observing the Atmosphere: An International Polar Year Legacy Consortium, *B. Am. Meteorol. Soc.*, 97, 1033–1056, <https://doi.org/10.1175/bams-d-14-00145.1>, 2016.
- 1030 World Meteorological Organization, World Meteorological Organization, and Global Atmosphere Watch: WMO/GAW aerosol measurement procedures: guidelines and recommendations., WMO/GAW, 2016.